Title

Osmium and lithium isotope evidence for weathering feedbacks linked to orbitally paced organic carbon burial and Silurian glaciations

Authors

Adam D. Sproson [a, b, *], Philip A. E. Pogge von Strandmann [c, d], David Selby [a, e], Emilia Jarochowska [f], Jiří Frýda [g, h], Jindřich Hladil [i], David K. Loydell [j], Ladislav Slavík [i], Mikael Calner [k], Georg Maier [f], Axel Munnecke [f], Timothy M. Lenton [l]

Affiliations

[a] Department of Earth Sciences, Durham University, Science Labs, Durham, DH1 3LE, UK.

[b] Biogeochemistry Research Center, Japan Agency for Marine-Earth Science and Technology, Yokosuka, Kanagawa 237-0061, Japan

[c] LOGIC, Institute of Earth and Planetary Sciences, University College London and Birkbeck, University of London, Gower Street, London, WC1E 6BT, UK.

[d] Institute of Geosciences, Johannes Gutenberg University, 55122 Mainz, Germany.

[e] State Key Laboratory of Geological Processes and Mineral Resources, School of Earth Resources, China University of Geosciences, Wuhan, 430074, Hubei, China.

[f] GeoZentrum Nordbayern, Friedrich-Alexander-Universität Erlangen-Nürnberg, Loewenichstraße 28, 91054 Erlangen, Germany

[g] Czech University of Life Sciences, Faculty of Environmental Sciences, Kamýcká 961/129, 165 21 Praha 6-Suchdol, Czech Republic.

[h] Czech Geological Survey, Klárov 3, 11821 Prague1, Czech Republic

[i] Institute of Geology of the Czech Academy of Sciences, Prague, Czech Republic

[j] School of the Environment, Geography and Geosciences, University of Portsmouth, Burnaby Road, Portsmouth PO1 3QL, UK.

[k] Department of Geology, Lund University, Sölvegatan 12, 223 62 Lund, Sweden.

[l] Global Systems Institute, University of Exeter, Laver Building (Level 8), North Park Road, Exeter, EX4 4QE, UK.

* corresponding author (adamsproson@gmail.com; sprosona@jamstec.go.jp)

Abstract

The Ordovician (~487 to 443 Ma) ended with the formation of extensive Southern Hemisphere ice sheets, known as the Hirnantian glaciation, and the second largest mass extinction in Earth History. It was followed by the Silurian (~443 to 419 Ma), one of the most climatically unstable periods of the Phanerozoic as evidenced by several large scale (> 5 ‰) carbon isotope ($\delta^{13}C$) perturbations associated with further extinction events. Despite several decades of research, the cause of these environmental instabilities remains enigmatic. Here, we provide osmium ($^{187}Os/^{188}Os$) and lithium ($\delta^{7}Li$) isotope measurements of marine sedimentary rocks that cover four Silurian $\delta^{13}C$ excursions. Osmium and Li isotope records resemble those previously recorded for the Hirnantian glaciation suggesting a similar causal mechanism. When combined with a new dynamic carbon-osmium-lithium biogeochemical model we suggest that astronomical forcing of the marine organic carbon cycle, as opposed to a decline in volcanic arc degassing or the rise of early land plants, resulted in drawdown of atmospheric CO_2, triggering continental scale glaciation, intense global cooling and eustatic sea-level lows recognised in the geological record. Lower atmospheric pCO_2 and temperatures during the Hirnantian and Silurian glaciations suppressed CO_2 removal by silicate weathering, driving $^{187}Os/^{188}Os$ and $\delta^{7}Li$ variability, supporting the existence of climate-regulating feedbacks.

Keywords: Osmium isotopes ($^{187}Os/^{188}Os$), Lithium isotopes ($\delta^{7}Li$), Silurian palaeoclimate, Hirnantian glaciation, Orbital obliquity, eccentricity and precession, Silicate weathering.

1. Introduction

The Earth's ecosystems underwent profound changes during the Ordovician and Silurian. Global cooling towards present-day equatorial sea surface temperatures (Trotter et al., 2008) coupled to a rise in atmospheric O_2 led to an abrupt increase in marine diversity during the Great Ordovician Biodiversification Event (Rasmussen et al., 2019). Increased volcanism during the Katian led to a gradual decline in biodiversity toward the end of the Ordovician, terminating with the Late Ordovician mass extinction (Rasmussen et al., 2019). This first of the Phanerozoic 'Big Five' extinctions coincided with the initiation of icehouse conditions and the extensive expansion of Southern Hemisphere continental ice, the Hirnantian glaciation (Algeo et al., 2016). A return to rapid biodiversity accumulation rates did not occur in the Silurian (Rasmussen et al., 2019), which was characterised by environmental instabilities linked to both minor and significant extinctions such as the 'Ireviken', 'Mulde', 'Lau' and 'Silurian-Devonian Boundary' bioevents (Fig. 1I; Calner, 2008).

The Hirnantian glaciation and Late Ordovician mass extinction are linked to a long-term decline in global temperatures brought about by some combination of: the enhanced weatherability of silicates, related to land-plant colonisation (Lenton et al., 2012) and/or the passage of fresh volcanic material through the tropics (Nardin et al., 2011); a reduction in volcanic arc degassing (McKenzie et al., 2016; Pogge von Strandmann et al., 2017); and/or an increase in organic carbon burial (Sproson, 2020). Although these processes continued to influence global climate well into the Silurian (Lenton et al., 2016; McKenzie et al., 2016; Nardin et al., 2011; Page et al., 2007), some explanations for Silurian bioevents have invoked a shift between two stable oceanic-climate states, driven by latitudinal changes in deep-water

formation (Jeppsson, 1990), or variations in global precipitation rates and continental runoff (Bickert et al., 1997). However, both the end-Ordovician and the Silurian extinction events are marked by similar variations in global $\delta^{13}C$ (Fig. 1J), oxygen isotopes ($\delta^{18}O$; Fig. 1L), eustatic sea-level (Fig. 1M) and lithological records (Calner, 2008; Munnecke et al., 2003), suggesting a similar causal link.

It has been postulated that Silurian climatic change and extinction events could have been driven by glacial expansion over Gondwana (Frýda et al., 2021; Munnecke et al., 2010; Trotter et al., 2016), much like the Late Ordovician that preceded it, astronomically paced by the ~4.5 Myr amplitude modulation of the cyclic eccentricity (400 kyr and 100 kyr) or obliquity (41 kyr) parameters of the Earth's axial motion and orbit (Sproson, 2020). Astronomical forcing of Silurian climate is supported by graptoloid turnover rates from the Late Ordovician to latest Silurian which correlate to the ~2.6 Myr eccentricity and ~1.3 Myr obliquity cycles (Crampton et al., 2018). Moreover, high resolution stratigraphic records for the Hirnantian glaciation suggest multiple glacial maxima paced by the ~1.2 Myr axial obliquity (Ghienne et al., 2014) or the ~100 kyr eccentricity (Sutcliffe et al., 2000) cycles. However, the lack of glacial sedimentary rocks in the post-Sheinwoodian stratigraphic record (Fig. 1K) has prevented the extension of astronomically paced glaciations as an explanation for Silurian climate events (Caputo et al., 1998; Díaz-Martínez and Grahn, 2007; Grahn and Caputo, 1992), despite indirect evidence of glaciation from dramatic facies changes in the Ludfordian which indicate a rapid worldwide shallowing (Frýda et al., 2021; Loydell and Frýda, 2011). Here, we provide Os and Li isotope records of sedimentary rocks – proxies for weathering processes and provenance – and a new dynamic carbon-osmium-lithium-model to test hypotheses for the cause(s) and nature of the Silurian events.

1.1 Tracing weathering using Os and Li isotopes

100 The Re-Os system undergoes parent-daughter fractionation during mantle melting leading to
101 more radiogenic $^{187}Os/^{188}Os$ values in the upper continental crust relative to recent mantle
102 derived minerals (Peucker-Ehrenbrink and Ravizza, 2000). The $^{187}Os/^{188}Os$ values of rivers
103 are therefore seen to reflect the provenance of continental weathering, from the silicate
104 weathering of unradiogenic juvenile basaltic minerals ($^{187}Os/^{188}Os$ = ~0.12) through to the
105 oxidative weathering of highly radiogenic organic-sulphide-rich rocks ($^{187}Os/^{188}Os$ = ~1.37)
106 (Georg et al., 2013). Stable Li isotopes, on the other hand, show limited fractionation during
107 magmatic processes, and the primary components of the upper continental crust therefore
108 display a narrow range of compositions (continental crust = ~0.6 ± 0.6 ‰, basalt = 0 to 5 ‰)
109 (Sauzéat et al., 2015). However, Li isotopes fractionate significantly during chemical
110 weathering, with the retention of ^{6}Li in weathering residues causing the $\delta^{7}Li$ values of rivers
111 (2 to 44 ‰) to reflect 'weathering congruency', defined as the ratio of primary rock
112 dissolution (congruent weathering drives rivers to low $\delta^{7}Li$), to secondary mineral (e.g.,
113 clays) formation (incongruent weathering drives rivers to high $\delta^{7}Li$) (Huh et al., 1998; Pogge
114 von Strandmann et al., 2017).
115 The respective $^{187}Os/^{188}Os$ and $\delta^{7}Li$ of organic-rich shales and carbonates record the
116 isotopic composition of seawater at the time of deposition (Peucker-Ehrenbrink and Ravizza,
117 2000; Pogge von Strandmann et al., 2017). In the modern oceans, the $^{187}Os/^{188}Os$ and $\delta^{7}Li$ of
118 seawater ($^{187}Os/^{188}Os$ = ~1.06, $\delta^{7}Li$ = ~31 ‰) reflect the balance between riverine inputs
119 ($^{187}Os/^{188}Os$ = ~1.54, $\delta^{7}Li$ = ~23 ‰), hydrothermal inputs ($^{187}Os/^{188}Os$ = ~0.12, $\delta^{7}Li$ = ~7
120 ‰), cosmogenic inputs ($^{187}Os/^{188}Os$ = ~0.13), and outputs related to the incorporation of Li
121 into low-temperature marine clays, which impose a fractionation of ~15 ‰, and the
122 scavenging of Os by organic or particulate matter (Misra and Froelich, 2012; Peucker-
123 Ehrenbrink and Ravizza, 2000). The residence time of Os (~10-60 kyr) and Li (~1.2 Myr) in
124 the ocean has allowed variations in these inputs and outputs, inferred from changes in the

125 sedimentary records of seawater $^{187}Os/^{188}Os$ and $\delta^{7}Li$, to provide unparalleled information
126 concerning the response of weathering to climatic and geological events (Misra and Froelich,
127 2012; Peucker-Ehrenbrink and Ravizza, 2000).
128
129 **2. Materials and methods**
130 **2.1 Palaeogeographic setting and sampling strategy**
131 To explore the response of weathering to climatic change during Silurian bioevents we
132 determined the respective $^{187}Os/^{188}Os$ and $\delta^{7}Li$ composition of three shale sections and three
133 carbonate sections that span much of the Silurian and include significant positive $\delta^{13}C$
134 excursions and extinctions: early Sheinwoodian (Aizpute-41 core, Latvia; Lusklint &
135 Lickershamn, Sweden); mid-Homerian (Bartoszyce core, Poland; Hunninge-1 core, Sweden);
136 and mid-Ludfordian (Kosov, Czech Republic), and the $^{187}Os/^{188}Os$ composition of a further
137 shale section (Klonk core, Czech Republic) that spans the Přídolí-Lochkovian boundary (see
138 *Supplementary Material*). Carbonate sections from Gotland (Sweden) and shale sections from
139 Latvia and Poland were respectively deposited in the shallow- and deep-waters of an
140 epicontinental sea to the north of the Rheic Ocean, whereas sections from the Czech Republic
141 represent deeper shelf sediments from the north coast of Gondwana, to the south of the Rheic
142 ocean (Fig. 1A).
143
144 **2.2 Sample preparation**
145 Prior to crushing, 20-80 g of shale samples were polished to eliminate contamination from
146 cutting and drilling marks and samples with any signs of veining or weathering were avoided.
147 The shale samples were then dried at 60 °C for ~12 h before being broken into chips with no
148 metal contact. Bulk carbonates and shales were crushed to a fine powder (~30 μm) in a
149 Zirconia ceramic dish using a shatterbox. Bulk carbonates were leached using a sequential

extraction method (Pogge von Strandmann et al., 2013), whereby ~0.1 g of carbonate was leached for 5 h at room temperature using Na acetate buffered to pH 5 by acetic acid. The sample preparation and Re-Os isotope and trace metal analysis were carried out at the Durham Geochemistry Centre (Laboratory for Sulfide and Source Rock Geochronology and Geochemistry) at Durham University. The Li isotope analysis was carried out at the stable isotope laboratory at the University of Oxford and later at the London Geochemistry and Isotope Centre at UCL.

2.3 Osmium isotope analysis of shales

Rhenium and Os abundances and isotopic compositions were determined using isotope dilution negative thermal ionisation mass spectrometry using Cr^{VI}–H_2SO_4 digestion and solvent extraction ($CHCl_3$), micro-distillation and anion chromatography methods (Creaser et al., 1991; Cumming et al., 2013; Selby and Creaser, 2003). The Cr^{VI}–H_2SO_4 digestion employed here principally dissolves the organic fraction of a shale, thus liberating the hydrogenous Re-Os load of the sediment and therefore avoiding detrital contamination (Selby and Creaser, 2003). The isolated Re and Os fractions were loaded onto Ni and Pt filaments respectively, and their isotopic composition was determined using a ThermoScientific TRITON mass spectrometer using Faraday collectors and the secondary electron multiplier, respectively.

Total procedural blanks for Re and Os are 10.09 ± 0.99 and 0.11 ± 0.06 pg respectively, with an average $^{187}Os/^{188}Os$ of 0.77 ± 0.54 (1SD; n=5). Raw Re and Os oxide values were corrected for oxygen contribution and mass fractionation. Calculated uncertainties include those associated with mass spectrometer measurements, blank abundance and isotopic composition, spike calibration, and sample and spike weights. In-house standard solutions of Re and Os (DROsS) yield an average $^{185}Re/^{187}Re$ value of

175 0.59872 ± 0.00135 (1SD, n = 24), and $^{187}Os/^{188}Os$ of 0.16101 ± 0.000401 (1SD, n = 41),
176 respectively, which is identical to previously published values (Nowell et al., 2008).
177 Initial $^{187}Os/^{188}Os$ ($^{187}Os/^{188}Os_i$) values in this study were determined from Re-Os data
178 and the ^{187}Re decay constant ($1.666e^{-11}$ a^{-1}) (Smoliar et al., 1996) and interpolated graptolite
179 biozone ages (Fig. S8). Analytical uncertainty for individual calculated Os_i is < 0.05. The
180 reproducibility of calculated $^{187}Os/^{188}Os_i$ was based on 15 analyses of the USGS rock
181 reference material SBC-1 (Bush Creek Shale) which has a value of ~0.65 ± 0.07 (2SD; Table
182 S4). Calculated $^{187}Os/^{188}Os_i$ ratios assume closed system behaviour after deposition and
183 therefore reflects the isotope composition of the local seawater at the time of sediment
184 deposition.
185
186 **2.4 Lithium isotope analysis of bulk carbonates**
187 A split of each sample solution was retained for cation analysis using an Elan Quadrupole
188 inductively coupled plasma mass spectrometer. Samples were matrix matched to 10 μg/g Ca
189 and calibrated against a set of synthetic standards made up from single element solutions. The
190 Al/Ca and Mn/Ca ratios were monitored to detect the influence of Li leached from clays.
191 Previous work suggests that carbonates must be >0.8 mmol/mol before carbonate Li isotope
192 ratios become measurably perturbed by Li leached from clays (Pogge von Strandmann et al.,
193 2013). Accuracy and precision were assessed by repeated analyses of seawater, JLs-1, and
194 repeated dissolutions of the Plenus Marl from Eastbourne. Sample reproducibility of Li/Ca
195 and Al/Ca was ~7% (2 SD, n=6). The larger part of each sample (typically containing 5-10
196 ng Li) was purified by passing it through a two-stage cation-exchange procedure (Pogge von
197 Strandmann et al., 2017; Pogge von Strandmann et al., 2019). Given that Li isotopes
198 fractionate during cation chromatography, it is critical to have column yields close to 100%.

To assess the efficacy of this process, splits of the solution were collected before and after the collected bracket for Li, which were shown to have <0.1% of Li.

The total procedural blank for Li isotope analysis is ~0.02 ng Li, which is insignificant compared to the mass of sample used. Analyses were performed on a Nu Plasma HR multi-collector ICP-MS at Oxford, and a Nu Plasma 3 MC-ICP-MS at UCL, using a sample-standard bracketing system relative to the LSVEC standard (Flesch et al., 1973). Each sample was measured three separate times during the same analytical session. Each individual measurement consisted of 10 ratios (10 s total integration time), giving a total integration time of 300 s/sample. At an uptake rate of 75 µl/min, the sensitivity for a 20 ng/ml solution is ~180 pA of ^{7}Li at Oxford (Pogge von Strandmann et al., 2019). Background instrumental Li intensity, typically ~0.01 pA, was subtracted from each measurement. Accuracy and external reproducibility, as assessed from seawater, is 31.1 ± 0.6 ‰ (2 SD, n = 16). Precision was also assessed from repeated analyses of an in-house marl standard, which also gives a reproducibility of ± 0.6 ‰ (n = 7). At UCL, a 5 ng/ml solution gives around 120 pA of ^{7}Li.

2.5 Dynamic C-Os-Li geochemical model

We developed a simple coupled carbon-cycle-climate model to explore potential drivers of new (^{187}Os/^{188}Os, δ^{7}Li) and existing (δ^{13}C, δ^{18}O) isotope data over relatively short-term events in the Silurian. The carbon cycle component of the model is based on the GEOCARBSULF (Berner, 2006) and COPSE (Lenton et al., 2018) biogeochemical models, and the simple model used by Pogge von Strandmann *et al.* (2017) to study the Hirnantian, adding osmium cycling (Lechler et al., 2015; Pogge von Strandmann et al., 2013) to the existing lithium cycle. In essence, the model interactively captures the long-term inorganic carbon cycle with degassing input of CO_2, and any imbalance in the organic carbon cycle

such as carbon burial, assumed to be balanced by CO_2 drawdown from silicate weathering. Silicate weathering depends on CO_2, temperature, and vegetation, providing negative feedback on climate variations. Silicate weathering, along with hydrothermal activity, drives input fluxes of Li and Os to the ocean and is balanced by sedimentary removal. A threshold response model is also considered to generate large (~5 ‰) $\delta^{13}C$ variations via the growth and decay of the marine organic carbon reservoir (Laurin et al., 2015), driven by numerical solutions for orbital precession and obliquity (Laskar et al., 2004). The climate component of the model – capturing changes in global temperature and ice sheet extent – is based on a logarithmic relationship between CO_2 and radiative forcing from the GCM-ice sheet modelling results of Pohl *et al.* (2016). The model is solved numerically using Euler's method run from initial values (Table S3) at a timestep of 5000 years. A detailed description of the model can be found in the *Supplementary Material*.

Key parameter settings for initialising the model are the rates of tectonic degassing and uplift, the areal coverage of land plants, and their effect on weathering. Normalised forcing factors for degassing (D), uplift (U), vegetation (V) and weathering (W) are derived from the COPSE and GEOCARBSULF biogeochemical model estimates for the Silurian (see Fig. 3 in Lenton et al. (2018)). Degassing was elevated relative to the present and we use an estimate for the start of the Silurian at ~443 Ma (D = 1.5). Uplift was comparable to today's conditions, and we use an average estimate for the Silurian (U = 0.94). The first non-vascular plants had colonised the land surface during the Late Ordovician, establishing an assumed modest fractional coverage (V = 0.15) but with a substantial effect on weathering (W = 0.75), consistent with previous work (Pogge von Strandmann et al., 2017). A key difference from GEOCARBSULF, which has been explored in COPSE (Lenton et al., 2018), is that we assume a larger plant amplification effect on weathering today (k_v^{-1}) of a factor of 10 rather than a factor of 4. To test different hypotheses, the model is either perturbed after 0.5 Myr by

changing forcing factors D, U, V or W, or subjected to orbital forcing from numerical solutions for precession or obliquity.

3. Results and discussion

3.1 Os and Li isotope records for the Silurian

New $^{187}Os/^{188}Os$ and $\delta^{7}Li$ profiles for these sections have been compiled with existing $\delta^{13}C$ and $\delta^{18}O$ profiles and show similar trends for each time period studied, but with differing magnitudes of change (Fig. 1B-1H and S1-S7; Table S1-S2). Prior to a $\delta^{13}C$ excursion there is a positive shift of magnitude 0.19 to 0.56 in the $^{187}Os/^{188}Os$ composition, often associated with a positive shift in $\delta^{18}O$ of magnitude 0.55 to 1.74 ‰. This is followed by a decline in the $^{187}Os/^{188}Os$ composition to pre-excursion values. During the $\delta^{13}C$ excursions, of magnitude 0.9 to 8.29 ‰, the $^{187}Os/^{188}Os$ composition generally remains low. In contrast, the $\delta^{7}Li$ of carbonates displays a positive shift of magnitude 4.7 to 9.6 ‰. During a plateau in $\delta^{13}C$ values, the $\delta^{18}O$ and $\delta^{7}Li$ values begin to return to pre-excursion values in some sections. During this decline, the $^{187}Os/^{188}Os$ values observe a second positive shift of magnitude 0.26 to 0.8 before returning to pre-excursion values either synchronously with the descending limb of the $\delta^{13}C$ record or prior to it.

Processes that could cause these variations include contamination during sample processing, diagenesis, or a primary seawater signal driven by changes in Earth system processes. Contamination of Re and Os from the detrital fraction of shales was avoided by using the CrO_3–H_2SO_4 digestion method, while cation exchange or leaching of clays, which could impart an isotopically light $\delta^{7}Li$ signal, was monitored by analysing cation/Ca ratios of carbonates. Diagenesis can be discounted because the shale sections studied here show no signs of veining or metamorphism suggesting that the extracted organic-phase-Os remains unaltered (Selby and Creaser, 2003) and cation/Ca ratios display no discernible trend with

δ^7Li (Table S2). Furthermore, δ^{13}C and δ^{18}O values in studied profiles (Fig. S1-S7) show similar values to other correlated sections that span the same intervals (Fig. 1J and 1L). It is therefore suggested that the isotopic shifts in the shale and carbonate sections represent primary seawater signatures.

When compiled onto our new age-depth model (Fig. S8), variations in $^{187}Os/^{188}Os$ and δ^7Li from this study (Fig. 2B-E) compare well, in terms of magnitude and timing of change, to records for the Hirnantian (Fig. 2A) suggesting similar causal processes. In general, we observe two peaks of radiogenic $^{187}Os/^{188}Os$ (centred around the vertical grey dashed line) separated by ~270-700 kyr (mean = 550 kyr; σ = 180) and an ascending limb of δ^7Li toward peak values (vertical black dashed line), which occurs ~210-630 kyr (mean = 450 kyr; σ = 180) after the first peak in radiogenic $^{187}Os/^{188}Os$ (Fig. 2). These broadly consistent patterns of change provide a target for numerical modelling. We use the model to test a series of hypotheses, attempting to reproduce: (1) the double-peaked $^{187}Os/^{188}Os$ response of magnitude 0.2 to 0.8; (2) a single transient peak of δ^7Li (>5 ‰); (3) $\delta^{13}C_{carb}$ variation of ~2-8 ‰ over ~1 to 2.5 Myr (Fig. 1J); (4) $\delta^{18}O_{phos}$ variation of ~1-2 ‰ over ~1 to 2 Myr (Fig. 1L); and, (5) sea-level drops of ~50-200 m over ~1 Myr (Fig. 1M).

3.2 Initial state of the C-Os-Li geochemical model

The relatively low plant cover of the Silurian, and corresponding suppression of the large assumed effect of plants on weathering, produces a high steady state CO_2 at ~16 PAL (and a global temperature relative to the present day, ΔT, of ~9K), which is consistent with the lack of a large, permanent ice sheet from the climate-ice sheet simulations of Pohl *et al.* (2016) for the Late Ordovician. A modest ice sheet extent of ~2 Mkm^2 is predicted and fixed at this value in the model variant without interactive ice sheets. The initial model state is poised to grow an ice sheet if that option is included and CO_2 declines, which is reasonable given that

299 the Hirnantian experienced a pronounced ice age. Initialising the model with higher D, lower
300 U, V, or W, would all tend to increase the initial CO_2 making it harder to trigger glaciation.
301 In the initial state the ocean Li reservoir is ~4 x 10^{16} mol, δ^7Li_{sw} = 17.5 ‰, and
302 δ^7Li_{carb} = 13.5 ‰, higher than the data, but close to the minimum allowable from isotopic
303 mass balance (Fig. 1F to H). The Os reservoir is ~1 x 10^8 mol with a $^{187}Os/^{188}Os$ of 0.64, in
304 the range of the data (Fig. 1B to E). An initial $\delta^{13}C$ of 1 ‰ is a reasonable baseline value for
305 the Silurian (Fig. 1J). We begin by testing the hypotheses previously proposed as drivers of
306 Hirnantian climate change, notably a decline in volcanic arc degassing and the colonisation
307 of land plants, before considering orbital forcing of imbalances in organic carbon burial and
308 the possibility of widespread Southern Hemisphere glaciations.
309
310 **3.3 Can tectonic or biological forcing explain observed Os and Li isotope records?**
311 Variations in the δ^7Li of seawater during the Hirnantian (Fig. 2A) have been linked to a
312 decrease in silicate weathering caused by a decline in global temperatures, ultimately linked
313 to a decline in CO_2 degassing. Continental arc volcanism continued to decline into the
314 Silurian (McKenzie et al., 2016) as the Iapetus Ocean closed during the formation of
315 Laurussia suggesting a possible link between degassing and our Os and Li isotope records.
316 An extreme halving of degassing over 1 Myr (Fig. 3A), which is unprecedented for the
317 Phanerozoic, causes a halving of atmospheric CO_2 and a global cooling of ~4 °C (Fig. 3B),
318 driving an increase in $\delta^{18}O_{phos}$ of 0.8 ‰ (Fig. 3C). A halving of the riverine and hydrothermal
319 fluxes coupled to a reduction in the oceanic Li reservoir drives a ~3 ‰ positive δ^7Li
320 excursion over ~3 Myr (Fig. 3C). Ocean Os content drops more rapidly, and because the
321 unradiogenic hydrothermal and basalt weathering input halves, whilst relatively radiogenic
322 sediment weathering remains constant, the $^{187}Os/^{188}Os$ of seawater increases by ~0.19 (Fig.
323 3C). Although O, Li and Os variation is in the same direction as Silurian records, the

variation is too small and not transient (Fig. 2 and 1L), displaying a permanent shift to higher values (Fig. 3C). This suggests that even an abrupt and rapid decline in degassing cannot (on its own) explain the Li and Os isotope variations during the Silurian (or Hirnantian) events and transient changes in degassing are assumed not to be applicable for the timescales under consideration.

The evolution of non-vascular land plants had a potentially profound effect on silicate weathering fluxes during the Late Ordovician (Lenton et al., 2012). In the Silurian, their spread was augmented by the evolution of the first vascular land plants (Lenton et al., 2016). Conceivably, expansions in plant cover and associated increases in global weathering rates occurred during the Silurian (Lenton et al., 2016), albeit of uncertain magnitude. Modelling an extreme doubling of vegetation cover over 1 Myr (Fig. 3D) causes CO_2 to decline by ~2.5 PAL, a < 2°C cooling (Fig. 3E) and a stepwise increase in $\delta^{18}O$ (Fig. 3F). The increase in silicate weathering, by ~10 % until CO_2 and temperature have adjusted, brought on by land plant proliferation drives a transient negative ~0.6 ‰ excursion in $\delta^{7}Li$ (Fig. 3F) because the unfractionated riverine source increases. The weathering of more radiogenic granitic and sedimentary rocks drives a similar transient decrease in the $^{187}Os/^{188}Os$ of ~0.02 (Fig. 3F). Neither isotopic response is in the direction observed in Silurian records (Fig. 2).

If we include an intensification of pedogenesis and clay formation via incongruent weathering, the riverine $\delta^{7}Li$, and therefore oceanic $\delta^{7}Li$, can increase, but this shift is no longer transient and the $^{187}Os/^{188}Os$ of seawater is unaffected. Increasing and then decreasing V, to represent phases of plant colonisation and associated weathering spikes (Lenton et al., 2016), can cause a small decrease then a small increase in $^{187}Os/^{188}Os$. However, even these large and rapid changes in plant cover cannot (alone) explain the Li and Os isotope variations during Late Ordovician and Silurian events (Fig. 2). Varying D (Fig. S9) or V (Fig. S10) alters the magnitude or duration of change, but it does not affect the overall modelled trends,

which do not compare favourably to observed records. It seems more likely that a modest, slower expansion of vegetation and/or decline in degassing could have helped 'prime' the Earth system to undergo the observed events.

Enhanced weatherability of silicate rocks during the Taconic (Finlay et al., 2010) and Scandian (Munnecke et al., 2010) orogenies or the passage of volcanic rocks through the tropics during the Late Ordovician and/or Silurian (Nardin et al., 2011) could have led to significant variation in the Li and Os isotope systems. To generate the Li isotope variation seen during the Hirnantian, previous isotope modelling would require a seemingly implausible increase in uplift of ~65 % above modern levels or going from zero to roughly double the present day area of basalt (Pogge von Strandmann et al., 2017). Moreover, seawater $^{187}Os/^{188}Os$ and $\delta^{7}Li$ has been shown to be driven lower during basaltic eruptions associated with oceanic anoxic events (Lechler et al., 2015; Pogge von Strandmann et al., 2013). Therefore, plausible changes in tectonic and biological forcing, including reductions in volcanic arc degassing, expansions of terrestrial plants, orogeny or enhanced basaltic weathering fail to reconcile Os and Li isotope records or generate the required magnitude of change observed, suggesting that other causal mechanisms are required to explain isotopic variations during the Silurian.

3.4 Can orbital forcing of the organic carbon cycle explain Silurian isotope variations?

Black shale deposition in palaeotropical restricted and semi-restricted settings during the late Katian and early Rhuddanian is associated with widespread anoxia and high rates of organic carbon burial comparable to Mesozoic oceanic anoxic events (Melchin et al., 2013; Stockey et al., 2020), possibly linked to increased primary productivity from nutrients supplied by upwelling or the weathering of newly exposed glaciogenic sediments (Pohl et al., 2017). A similar pattern of black shale deposition or anoxic seafloor conditions continued until the

374 Ludlow (Page et al., 2007). Organic carbon burial on continental margins can influence
375 planetary climate and largely controls exogenic $\delta^{13}C$ values, displaying a strong correlation to
376 astronomical forcing (Kocken et al., 2019). Weaker forcing is associated with reduced
377 seasonality which drives higher annual precipitation and sediment accumulation, leading to
378 the burial of more isotopically light (^{12}C) organic carbon, and therefore higher seawater $\delta^{13}C$
379 values, and CO_2 sequestration, becoming reversed under stronger forcing (Kocken et al.,
380 2019). Additionally, lower seasonality is associated with oceanic cooling (high $\delta^{18}O$ values)
381 leading to the greater storage of organic carbon as biogenic methane ($\delta^{13}C = < -70$) in
382 submarine methane hydrates (Kocken et al., 2019). The cyclical nature of Late Ordovician to
383 Early Devonian $\delta^{13}C$ (Fig. 1J) and $\delta^{18}O$ (Fig. 1L) records has been linked to the long-term
384 ~4.5 Myr amplitude modulation of the Earth's ~400 kyr eccentricity and ~1.2 Myr obliquity
385 cycles, whereby prolonged intervals of exceptionally low forcing drove positive $\delta^{13}C$ and
386 $\delta^{18}O$ values via enhanced organic carbon burial, storage of biogenic methane and/or global
387 cooling (Sproson, 2020).

388 In order to obtain the observed > 1 ‰ variations in $\delta^{13}C$ on Myr-timescales, carbon
389 burial fluxes need to be tied to the development and decay of new carbon sinks, rather than
390 changes in carbon production and burial in existing carbon reservoirs (Laurin et al., 2015).
391 Here, we explore the potential of astronomically forced variations in marine organic carbon
392 reservoir stability as a driver of observed isotope variations. Following Laurin *et al.* (2015),
393 we assume that organic carbon moves via a series of quasi-stable reservoirs tied to the
394 efficiency of carbon burial relative to the intensity of carbon production. Below an obliquity
395 or precession threshold (th1), i.e., a period of low-amplitude insolation variation, the quasi-
396 stable reservoir of bulk organic carbon grows, sequestering atmospheric CO_2 and isotopically
397 light carbon. Between th1 and another threshold (th2), this reservoir remains stable. Above
398 th2, i.e., a period of high-amplitude insolation variation, the stored carbon is returned to the

399 exogenic reservoir as the bulk organic carbon reservoir decays, becoming a source of
400 atmospheric CO_2 and isotopically light carbon (see *Supplementary Material*). Numerical
401 astronomical models do not extend beyond 250 Ma and we therefore use sections of the
402 La2004 numerical model (Laskar et al., 2004) over the last 30 Ma (Fig. 4) as a representative
403 case for forcing Silurian palaeoclimate.

404 First, we consider obliquity forcing, using an illustrative exceptionally low obliquity
405 variation between 9.4 and 11.6 Ma (inset in Fig. 4C; Fig. 5A) to drive variations in the
406 stability of the marine sedimentary organic carbon reservoir (Fig. 5B). We assume that this
407 forcing can generate a ~5 ‰ variation in $\delta^{13}C$ (Fig. 5D), consistent with the larger Silurian
408 events recorded in the geological record (Fig. 1J), corresponding to the transient
409 accumulation of 8.5×10^4 Gt of carbon over 1.5 Myr (Fig. 5B). Such accumulation rates are
410 an order of magnitude higher than those used previously to simulate $\delta^{13}C$ variability during
411 the Cretaceous (Laurin et al., 2015). We justify this accordingly: (1) the Silurian experienced
412 a colder climate and a greater anoxic fraction of the ocean when compared to the Cretaceous
413 (Lenton et al., 2018) leading to higher levels of organic matter preservation; (2) the numerical
414 model of Laurin et al. (2015) did not account for any feedback mechanisms within the
415 carbon-cycle that would otherwise reduce the impacts of reservoir stability on planetary
416 climate; (3) we are attempting to simulate ~5 ‰ $\delta^{13}C$ variations as opposed to ~1 ‰
417 variations recorded in the Cretaceous; (4) we did not incorporate carbon storage in submarine
418 methane hydrates in our model, which would otherwise reduce accumulation rates.

419 Two maxima of organic carbon accumulation (Fig. 5B) are separated by the ~1.2 Myr
420 obliquity cycle (Fig. 5A), causing atmospheric CO_2 to decline from ~16 to ~10 PAL (Fig.
421 5C), like previous estimates for the Ordovician and Silurian (Lenton et al., 2018), before
422 obliquity forcing starts to generate net carbon release from the organic carbon reservoir (Fig.
423 5B). This corresponds to a cooling of ~2°C (Fig. 5C) and increase of ~0.5 ‰ in $\delta^{18}O_{phos}$ (Fig.

5D), smaller than variations in the conodont apatite record (Fig. 1L). The drop in atmospheric CO_2 and temperature leads to a reduction in silicate weathering, driving a decline in the ocean Os and Li reservoirs. The reduced weathering of unradiogenic silicates, such as basalt, by ~50 % relative to more radiogenic Os-rich lithologies such as sediments, leads to a ~0.1 increase in the $^{187}Os/^{188}Os$ of seawater (Fig. 5E), with peak values during minimum atmospheric pCO_2 (Fig. 5C). Meanwhile a reduction in the riverine Li flux drives a gradual increase of ~1.5 ‰ in the δ^7Li of seawater (Fig. 5E). The long ocean residence time of Li (~1.3 Myr in the model) relative to Os (~30 kyr in the model) leads to a more muted Li isotope response to climatic change when compared to Os isotopes. Although we capture the multiple peaks in Os isotopes relative to single peak in δ^7Li records, the magnitude of change is smaller and more protracted, the peaks are separated by ~1.2 Myr in the model whereas Silurian records are separated by ~0.2-0.7 Myr (Fig. 2).

Next, we consider precession forcing, using an illustrative period of exceptionally low precession variation between 9.6 to 10.6 Ma (inset in Fig. 4A; Fig. 5F) to drive variations in the stability of the marine organic carbon reservoir (Fig. 5G). This forcing can generate a similar magnitude of change to obliquity forcing (Fig. 5G-5J), but unlike obliquity forcing, the two maxima of organic carbon accumulation are separated by the ~400 kyr eccentricity cycle (Fig. 5F), leading to a transient accumulation of ~5 x 10^4 Gt of carbon over ~0.7 Myr (Fig. 5G). This places peaks in Os and Li isotopes (Fig. 5J) within the ~0.2 to 0.7 Myr range recorded in the data (Fig. 2). However, the large uncertainty associated with the age-depth model used here (Fig. 2) precludes us from discounting the influence of obliquity. Although the precession forced model improves on the obliquity model by giving a timing more consistent with the Os and Li isotope variation, the magnitude of change remains insufficient (Fig. 2). Hence, we consider an additional factor – the hypothesis that astronomical forcing of

448 the organic carbon cycle triggered intermittent glaciations during the Hirnantian and Silurian
449 (Sproson, 2020).
450
451 **3.5 Orbitally paced Silurian glaciations**
452 A decline in atmospheric CO_2 during the Late Ordovician led to extensive Southern
453 Hemisphere glaciation over Gondwana, associated with a glacio-eustatic sea-level change of
454 ~70-100 m, during the Hirnantian (Algeo et al., 2016). According to an Earth system model
455 for the Late Ordovician, there is a nonlinear response of southern hemisphere continental ice
456 sheet build-up to a decrease in radiative forcing (Pohl et al., 2016). At a pCO_2 of 16 PAL,
457 small ice caps begin to nucleate at the pole and high latitudes (≥ 60°S), but by 12 PAL ice
458 sheet feedback processes cause these sporadic glaciers to coalesce rapidly into a single
459 continental-scale ice sheet that extends to mid latitudes (45°S) where it remains relatively
460 stable. This transition corresponds to a global cooling of ~4°C and high climate sensitivity of
461 >9°C for a doubling/halving of atmospheric CO_2.
462 Running the previous obliquity (Fig. 6A) and precession forcing (Fig. 6G) of the
463 marine sedimentary organic carbon reservoir with an ice sheet and climate sensitivity derived
464 from Pohl *et al.* (2016) again leads to a transient accumulation of ~5-9 x 10^4 Gt of carbon
465 (Fig. 6B and 6H), generating a $\delta^{13}C$ variation of ~4.5-5 ‰ (Fig. 6E and 6K). With the
466 increased climate sensitivity, this drives a rapid cooling of ~4-5 °C (Fig. 6C and 6I) and an
467 increase in the Gondwanan ice sheet area of ~36 Mkm^2, expanding from ~90°S to ~45°S,
468 equating to a glacioeustatic drop of ~65 m (Fig. 6D and 6J). Subsequent net carbon loss can
469 generate a recovery of CO_2 to ~15 PAL, warming of ~4 °C, and shrinkage of ice sheets to ~5-
470 10 Mkm^3. Then, a further phase of net carbon accumulation causes CO_2 to decline to ~11
471 PAL, corresponding cooling of ~4 °C (Fig. 6C and 6I), and ice sheets again expanding to 36

472 Mkm^3 (Fig. 6D and 6J). Then, as eccentricity or obliquity variation increases again, net
473 carbon loss causes CO_2 to rise to ~18 PAL, eliminating ice sheets.
474 Projected cooling is comparable to estimated temperature anomalies of >5°C for the
475 Ludlow and Přídolí (Trotter et al., 2016) whilst modelled sea-level change is comparable to
476 reconstructed sea-level variations of 50-80 m during Silurian climate events (Fig. 1M).
477 Cooling coupled to an increase in ice volume, which directly influences the $\delta^{18}O$ of seawater,
478 leads to a $\delta^{18}O_{phos}$ increase of ~2 ‰ (Fig. 6E and 6K), similar to $\delta^{18}O$ perturbations recorded
479 in the Silurian conodont apatite record (Fig. 1L). Following a series of sensitivity tests, a
480 doubling of the average thickness of the ice sheet from 1 km to 2 km (Fig. 7A) increases the
481 magnitude of $\delta^{18}O_{phos}$ variability from ~2 ‰ to ~2.5 ‰ (Fig. 7C). Tripling the thickness of
482 the ice sheet to 3 km (Fig. 7D), consistent with Pohl et al.'s (2016) simulations, increases the
483 magnitude of $\delta^{18}O_{phos}$ variability to ~3.5 ‰ (Fig. 7F), consistent with conodont apatite
484 records for the Hirnantian (Trotter et al., 2008) and Mid-Ludfordian (Frýda et al., 2021), but
485 generally higher than other Silurian records (Trotter et al., 2016). An increase in ice thickness
486 to 2 and 3 km drives a larger sea-level drop of 120 m and 190 m, respectively (Fig. 7B and
487 7E). The former is comparable to sea-level estimates for the Hirnantian whilst the latter is far
488 higher than anything interpreted for the Ordovician and Silurian (Haq and Schutter, 2008).
489 This suggests that although the Hirnantian glaciation likely had an ice sheet thickness of up to
490 ~3 km, Silurian ice sheets were much smaller, reaching an average ice sheet thickness closer
491 to ~1 km, explaining the lack of marine terminating glaciers and the therefore glacial tillites
492 in the post-Sheinwoodian geological record (Fig. 1K) and low amplitude sea level variation
493 (Calner, 2008).
494 A reduced riverine flux of Os and Li, coupled to a shift to more incongruent
495 weathering due to increased clay formation caused by a longer continental residence time of
496 water, proposed for the Hirnantian glaciation (Pogge von Strandmann et al., 2017), causes an

497 increase in the $^{187}Os/^{188}Os$ of seawater and the δ^7Li of carbonate by ~0.13-0.2 and ~2.5-4.5
498 ‰, respectively (Fig. 6F and 6L), still substantially lower than recorded values (Fig. 2).
499 Although it is not possible to estimate the exact parameters governing the isotope systems
500 during the Palaeozoic, we speculate as to the possible causes of discrepancies between
501 modelled and observed data based on known processes. Physical erosion of Os-rich
502 sediments, such as shales and pyrite, in response to the expansion of large scale rock-grinding
503 glaciers has been shown to influence the Late Pleistocene Os record through the injection of
504 radiogenic Os to the ocean (Georg et al., 2013). Doubling sediment weathering (Fig. 7H)
505 with maximum ice sheet extent (Fig. 7G), to mimic the erosion of Os-rich lithologies,
506 increases the magnitude of the $^{187}Os/^{188}Os$ response to ~0.4 (Fig. 7I) on a similar order to
507 Silurian records (Fig. 2). The residence time of Li in the ocean is estimated to be ~1 to 1.5
508 Myr for the present day (Huh et al., 1998), but if we assume that the oceanic Li residence
509 time was half that of the present, due to a higher Li removal rate on continental margins with
510 a higher sediment accumulation rate than present (Fig. 7K), the δ^7Li of seawater increases by
511 ~4-5 ‰ (Fig. 7L). Additionally, if we assume that the δ^7Li of riverine inputs underwent a
512 larger fractionation of 20 ‰, due to even higher clay formation associated with the expansion
513 of ice sheets (Fig. 7M-N), the magnitude of the seawater δ^7Li response increases to ~7-10 ‰
514 (Fig. 7O).

515 Finally, numerical models used here generate multiple peaks in $\delta^{13}C$ tied to
516 eccentricity or obliquity minima (Fig. 6E, K) which are not clearly observed in $\delta^{13}C$ records
517 (Fig. 1J). This discrepancy could be an artefact of undersampling incomplete geological
518 sections, indicating the need for more complete Silurian $\delta^{13}C$ records. For example,
519 exceptionally complete sedimentary records for the Hirnantian reveal several $\delta^{13}C$ cycles
520 associated with glacial apices, similar to our model, that would otherwise be missing due to
521 hiatuses during sea level lowstands (Ghienne et al., 2014). Alternatively, simply forcing

organic carbon burial alone may be too simplistic to recreate the full complexity of records, and an interactive organic carbon cycle and/or additional forcing mechanisms, such as volcanic arc degassing or land-plant development, may be needed to reconcile numerical models with the geological record.

4. Conclusion

The $^{187}Os/^{188}Os$, $\delta^{7}Li$, $\delta^{13}C$, $\delta^{18}O$, and sea level response from our dynamic carbon-osmium-lithium-model can recreate the variability within Os and Li isotope records from this study and the magnitude of $\delta^{13}C$, $\delta^{18}O$ and sea-level records from the literature, combining all lines of evidence under one causal mechanism for the first time. We propose that the long-term ~4.5 Myr amplitude modulation of the Earth's orbital eccentricity and/or obliquity led to prolonged periods of high organic carbon burial, atmospheric CO_2 drawdown, cooling and continental glaciation during the Hirnantian, the early Sheinwoodian, the Homerian, the mid Ludfordian and the late Přídolí-early Lochkovian, extending the notion of 'Cenozoic-style' glacial cycles and high-order phenomena during the Late Ordovician (Ghienne et al., 2014) to the Silurian. Dramatic cooling or eustatic regression associated with glaciations and/or preceding marine anoxic/euxinic conditions would have removed the habitat space of marine taxa leading to extinctions including the Late Ordovician, 'Ireviken', 'Mulde', 'Lau' and 'Silurian-Devonian Boundary' events.

Due to the large uncertainty associated with the age model used in this study, and potential temporal aliasing arising from the under-sampling of incomplete geological sections, we are unable to determine whether eccentricity or obliquity was the dominant pace setter for Silurian glaciations. Future work should look to develop high resolution records with improved age control, akin to Ghienne et al. (2014), for the Silurian. Finally, the dynamic model developed in this study is too simplistic (see section 4.8 in the *Supplementary*

547 *Material*) to recreate the nuances of observed Hirnantian and Silurian records. More complex
548 modelling that includes a full description of the Earth's C-O-N-P-S cycles (e.g., Lenton et al.,
549 2018) and ice-sheet feedbacks (e.g., Pohl et al., 2016) is needed to fully reconcile the forcing
550 parameters explored here with Silurian records.
551
552 **Acknowledgements**
553 A.D. Sproson would like to thank the Geological Society of London's William George
554 Fearnsides fund and the College of St. Hild and St. Bede's (Durham University) John
555 Simpson Greenwell Memorial Fund for partially funding this research. P. A. E. Pogge von
556 Strandmann acknowledges financial support from the ERC grant 682760
557 CONTROLPASTCO2. D. Selby acknowledges support from the TOTAL Endowment Fund
558 and the Dida Scholarship of CUG Wuhan. J. Frýda was supported by GAGR (grant No. 17-
559 18120S). T.M. Lenton was supported by NERC (NE/N018508/1, NE/P013651/1). L. Slavík
560 was supported by GACR (grant No. GA17-06700S) and together with J. Hladil received
561 institutional support from RVO 67985831. Finally, we would like to thank T. Lyons and
562 three anonymous reviewers for their constructive comments which greatly improved this
563 manuscript.
564
565 **Appendix A. Supplementary material**
566 The supplementary material contains a description of the geological setting, supplementary
567 results, age-depth model, and the dynamic C-Os-Li geochemical model along with Table S1-
568 S3 and Fig. S1-S10. An excel version of the supplementary tables, including Re-Os data for
569 the USGS rock reference material SBC-1 (Table S4), and dynamic C-Os-Li geochemical
570 models used in this study are also provided.

571 **Figures**

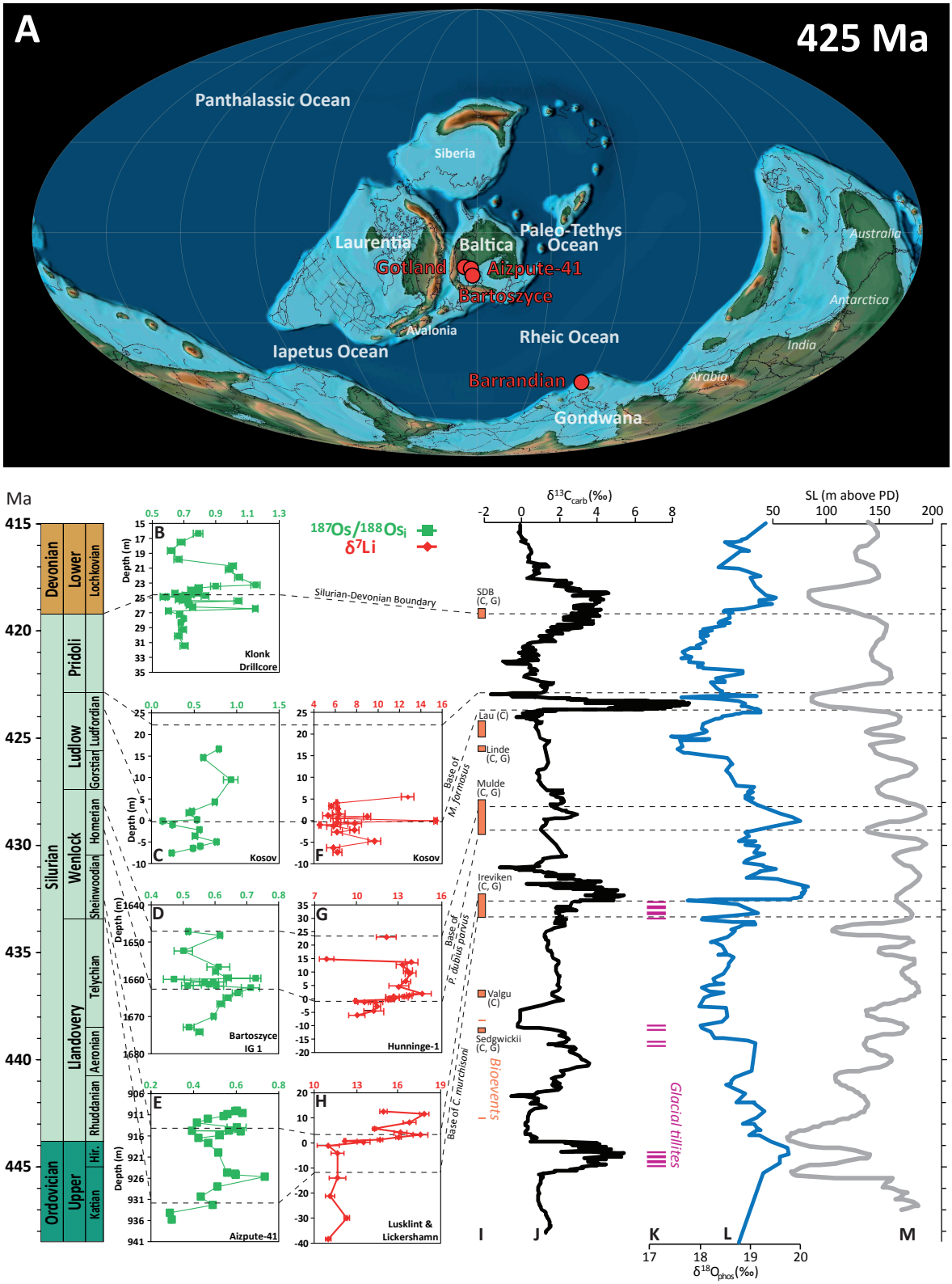

572 **Fig. 1.** Palaeoclimate records for the Upper Ordovician to the Lower Devonian. (**A**)

573 Palaeogeographic reconstruction of the Wenlock (425 Ma) with sample locations highlighted

574 by red circles (Scotese, 2016). Osmium (green squares) and δ^7Li (red diamonds) isotope data

575 are shown for the Klonk (**B**), Kosov (**C** and **F**), Bartoszyce IG-1 (**D**), Aizpute-41 (**E**),
576 Hunninge-1 (**G**), Lusklint (**H**) and Lickershamn (**H**) sections (see Fig. S1-S7 for more
577 details). Regional data sets from this study are compared to global conodont (C) and
578 graptolite (G) bioevents (**I**), carbonate $\delta^{13}C$ (**J**), glacial tillites (**K**) conodont apatite $\delta^{18}O$ (**L**)
579 and eustatic SL (**M**) records (Caputo et al., 1998; Díaz-Martínez and Grahn, 2007; Grahn and
580 Caputo, 1992; Haq and Schutter, 2008; Sproson, 2020; Trotter et al., 2008; Trotter et al.,
581 2016).
582

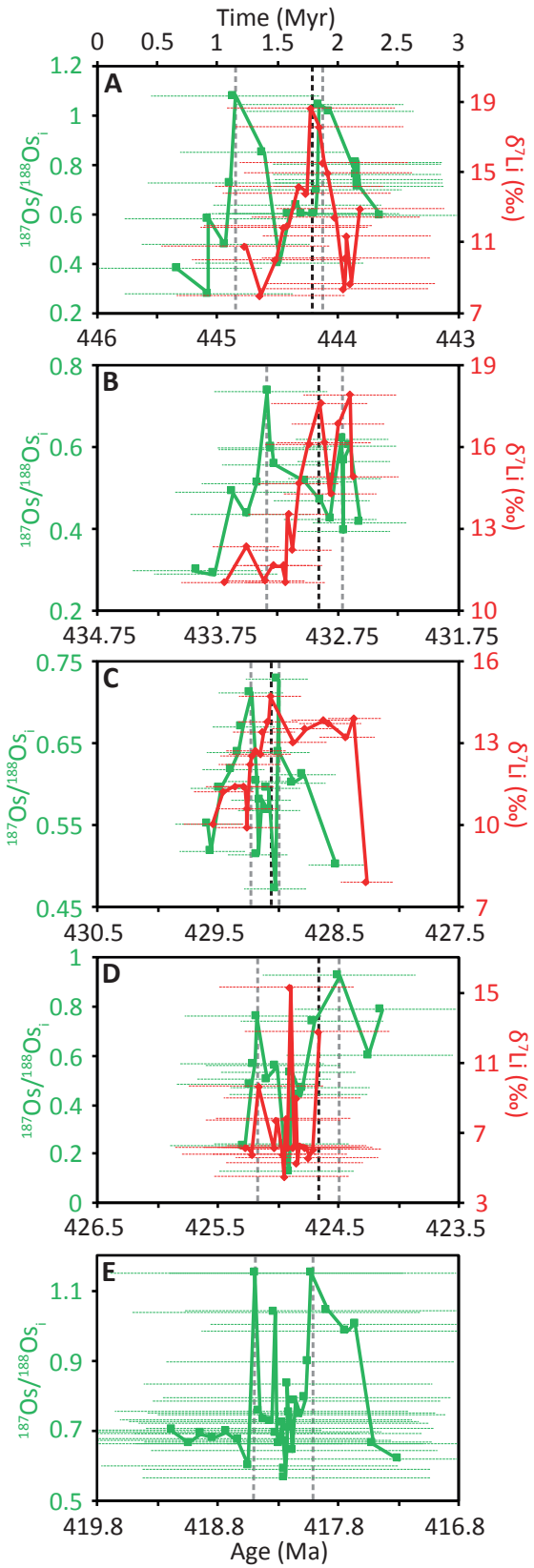

583 **Fig. 2.** Osmium and lithium isotope data for the Hirnantian (Finlay et al., 2010; Pogge von
584 Strandmann et al., 2017) (**A**), Telychian-Sheinwoodian boundary (**B**), mid-Homerian (**C**),
585 mid-Ludfordian (**D**) and Přídolí-Lochkovian boundary (**E**) compiled onto our new age-depth

model (Fig. S8). The vertical dashed grey and black lines highlight the key respective features of Os and Li isotope variation the dynamic carbon-osmium-lithium-model will attempt to recreate. The horizontal dashed lines represent 1σ age uncertainty for Os (green) and Li (red) isotope records.

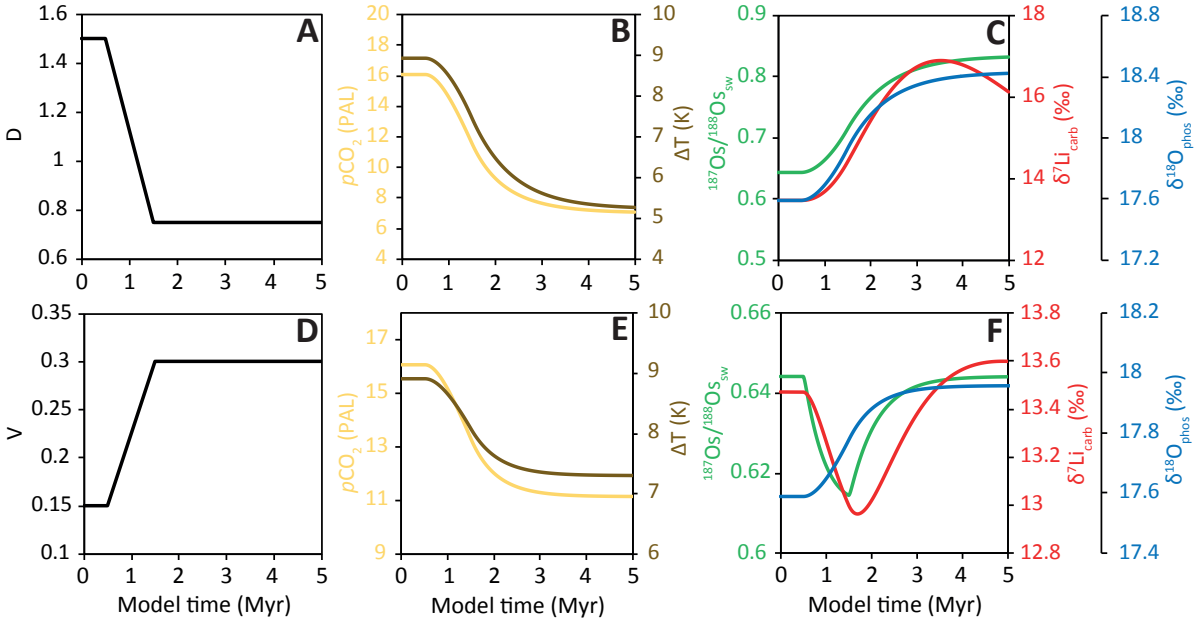

591 **Fig. 3.** The effect of degassing (A-C) and vegetation (D-F) on the O, Os and Li isotope systems

592 using a dynamic carbon-osmium-lithium-model.

593

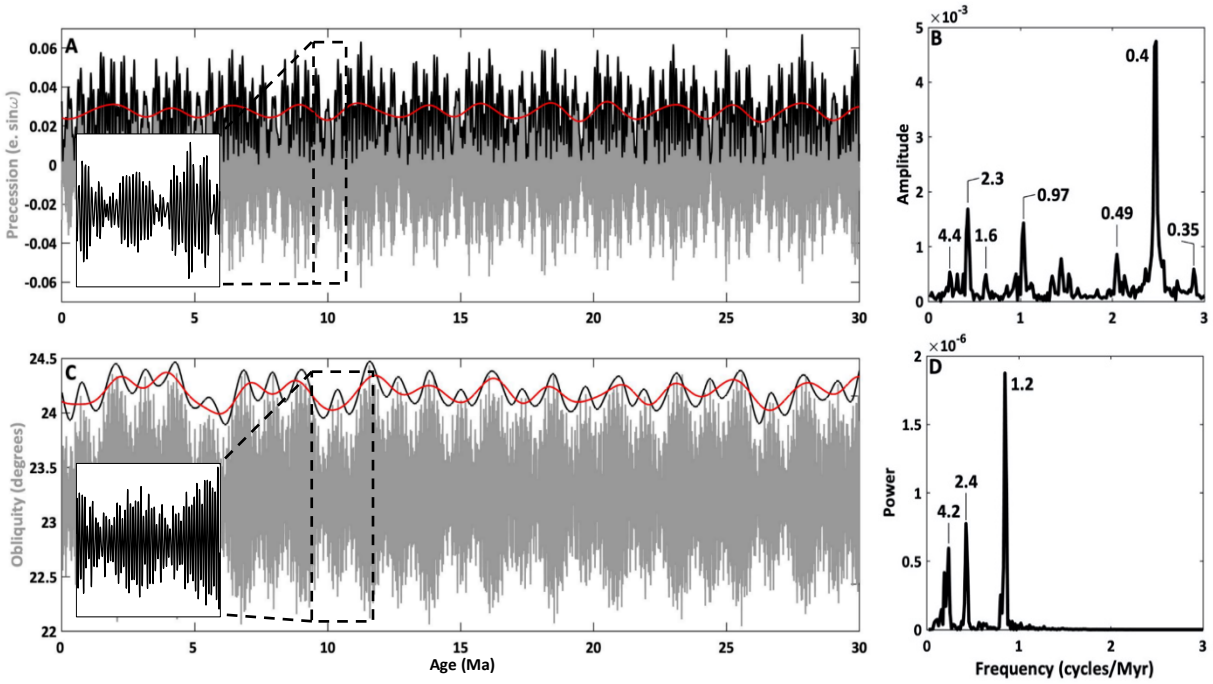

Fig. 4. Orbital records for the last 30 Myr**.** Precession (**A**) and obliquity (**C**) from the La2004 numerical model (grey) (Laskar et al., 2004) used to drive carbon-cycle models (inset of **A** and **B**). The eccentricity (**A**) and the amplitude modulation of obliquity (**C**) along with their ~2.4 Myr (0 to 0.7 cycles/myr) low pass filtering are show by black and red lines, respectively. A periodogram of the eccentricity (**B**) and the obliquity amplitude modulation (**D**) are shown along with dominant periods (Myr) (Sproson, 2020).

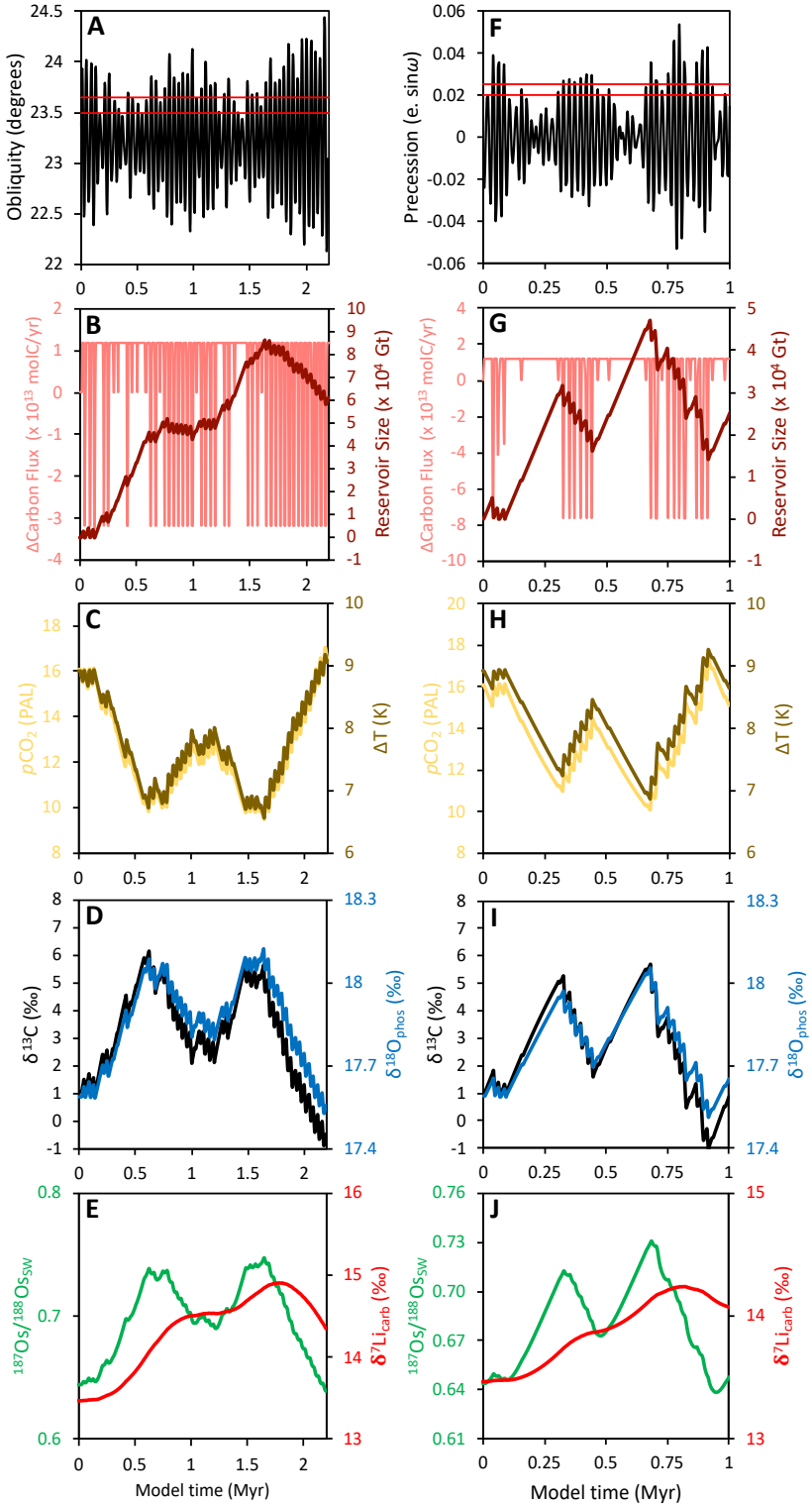

Fig. 5. The effect of an astronomically controlled quasi-stable reservoir on the C, O, Os and Li isotope systems. Modelled for a period of exceptionally low obliquity (**A**-**E**) and precession (**F**-**J**) variability using a dynamic carbon-osmium-lithium-model.

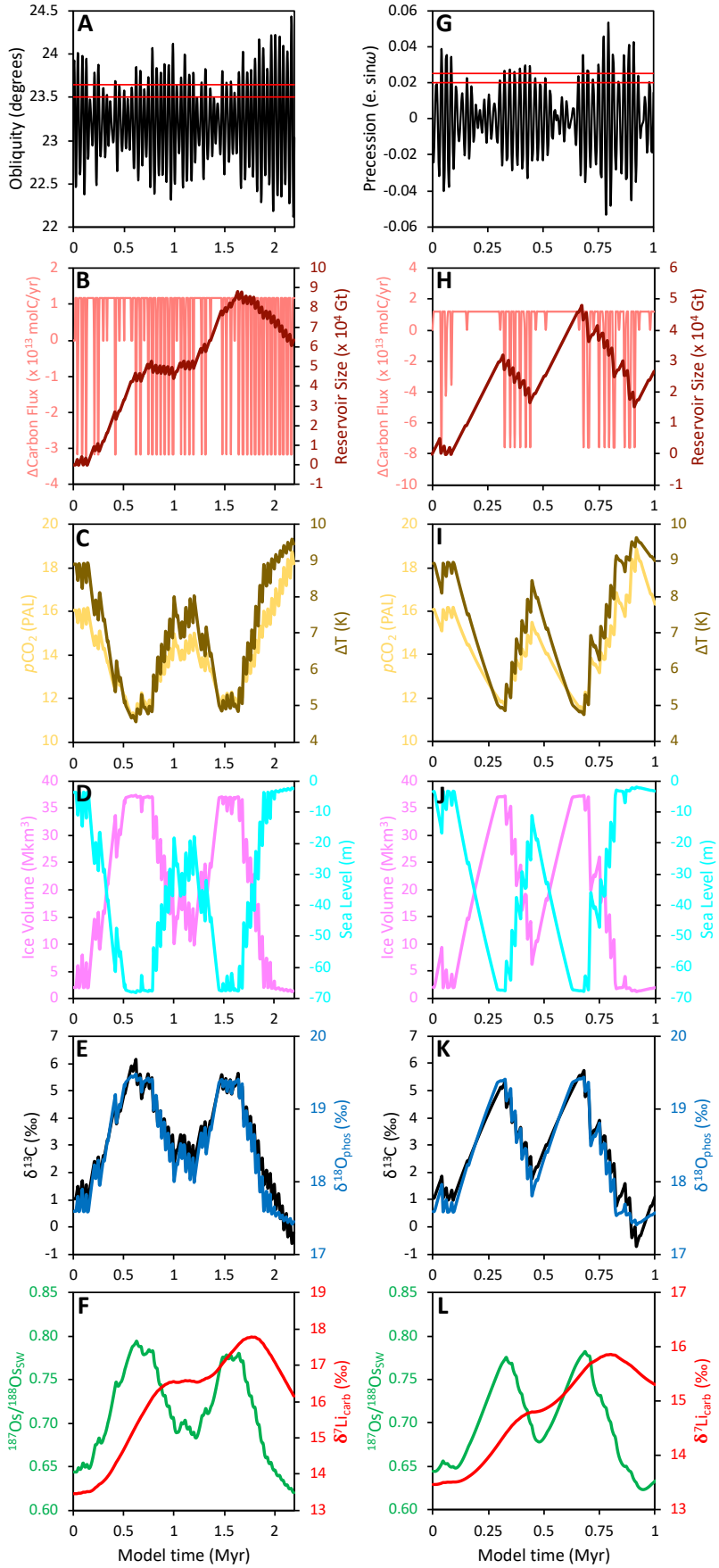

606 **Figure 6.** The effect of an astronomically controlled quasi-stable reservoir on the C, O, Os

607 and Li isotope systems for a period of exceptionally low obliquity (**A**-**F**) and precession (**G**-
608 **L**) variability. As opposed to scenarios presented in Fig. 3 and Fig. 5, the ice sheet and
609 climate sensitivity of Pohl *et al.* (2016) has been added.
610

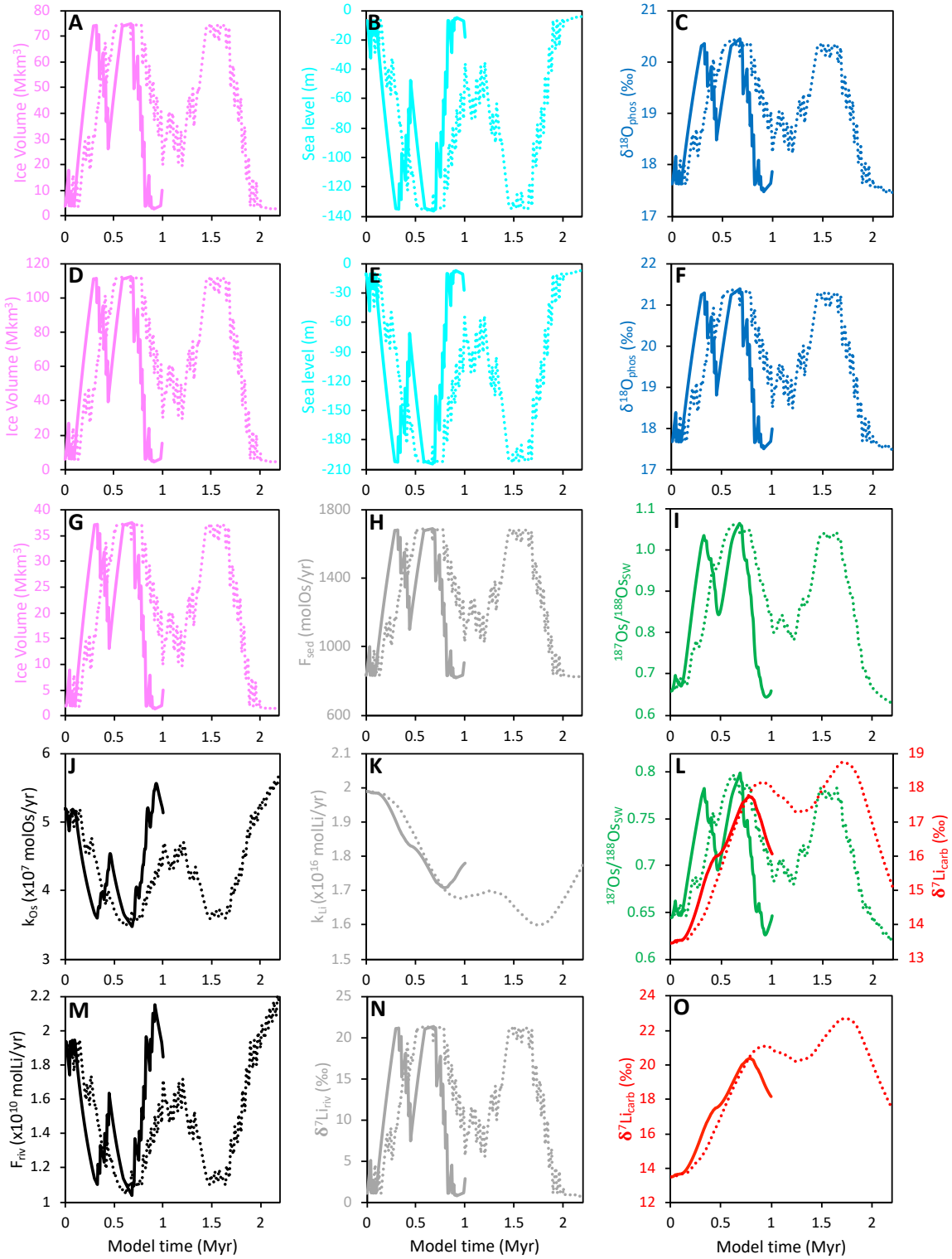

Fig. 7. Sensitivity studies for the effect of an astronomically controlled quasi-stable reservoir on the C, O, Os and Li isotope systems for a period of exceptionally low obliquity (dashed lines) and precession (solid lines) variability with the ice sheet and climate sensitivity of Pohl *et al.* (Pohl et al., 2016). Sensitivity studies are as follows: ice volume, sea level and $\delta^{18}O_{phos}$

for an ice sheet thickness of 2 km (**A-C**) and 3 km (**D-F**); the effect of tying ice volume (**G**) to sedimentary Os flux (**H**) on the $^{187}Os/^{188}Os$ of seawater (**I**) after replacing Eq. 29 with Eq. 31; the influence of doubling the partition coefficient (k) of Os (**J**) and Li (**K**) on the $^{187}Os/^{188}Os_{sw}$ and δ^7Li_{carb} values (**L**); the effect of increasing the fractionation factor of the Li riverine endmember to 20 ‰ (**M** and **N**) on δ^7Li_{carb} (**O**).

References

Algeo, T.J., Marenco, P.J., Saltzman, M.R., 2016. Co-evolution of oceans, climate, and the biosphere during the 'Ordovician Revolution': A review. Palaeogeography, Palaeoclimatology, Palaeoecology 458, 1-11.

Berner, R.A., 2006. GEOCARBSULF: A combined model for Phanerozoic atmospheric O2 and CO2. Geochimica et Cosmochimica Acta 70, 5653-5664.

Bickert, T., Pätzold, J., Samtleben, C., Munnecke, A., 1997. Paleoenvironmental changes in the Silurian indicated by stable isotopes in brachiopod shells from Gotland, Sweden. Geochimica et Cosmochimica Acta 61, 2717-2730.

Calner, M., 2008. Silurian global events – at the tipping point of climate change, in: Elewa, A.M.T. (Ed.), Mass Extinction. Springer Berlin Heidelberg, Berlin, Heidelberg, pp. 21-57.

Caputo, M.V., Landing, E., Johnson, M., 1998. Ordovician–Silurian glaciations and global sea-level changes. Silurian cycles, 15-25.

Crampton, J.S., Meyers, S.R., Cooper, R.A., Sadler, P.M., Foote, M., Harte, D., 2018. Pacing of Paleozoic macroevolutionary rates by Milankovitch grand cycles. Proceedings of the National Academy of Sciences 115, 5686-5691.

Creaser, R., Papanastassiou, D., Wasserburg, G., 1991. Negative thermal ion mass spectrometry of osmium, rhenium and iridium. Geochimica et Cosmochimica Acta 55, 397-401.

Cumming, V.M., Poulton, S.W., Rooney, A.D., Selby, D., 2013. Anoxia in the terrestrial environment during the late Mesoproterozoic. Geology 41, 583-586.

Díaz-Martínez, E., Grahn, Y., 2007. Early Silurian glaciation along the western margin of Gondwana (Peru, Bolivia and northern Argentina): Palaeogeographic and geodynamic setting. Palaeogeography, Palaeoclimatology, Palaeoecology 245, 62-81.

Finlay, A.J., Selby, D., Gröcke, D.R., 2010. Tracking the Hirnantian glaciation using Os isotopes. Earth and Planetary Science Letters 293, 339-348.

Flesch, G.D., Anderson, A.R., Svec, H.J., 1973. A secondary isotopic standard for 6Li/7Li determinations. International Journal of Mass Spectrometry and Ion Physics 12, 265-272.

Frýda, J., Lehnert, O., Joachimski, M.M., Männik, P., Kubajko, M., Mergl, M., Farkaš, J., Frýdová, B., 2021. The Mid-Ludfordian (late Silurian) Glaciation: A link with global changes in ocean chemistry and ecosystem overturns. Earth-Science Reviews 220, 103652.

Georg, R.B., West, A.J., Vance, D., Newman, K., Halliday, A.N., 2013. Is the marine osmium isotope record a probe for CO2 release from sedimentary rocks? Earth and Planetary Science Letters 367, 28-38.

Ghienne, J.-F., Desrochers, A., Vandenbroucke, T.R.A., Achab, A., Asselin, E., Dabard, M.-P., Farley, C., Loi, A., Paris, F., Wickson, S., Veizer, J., 2014. A Cenozoic-style scenario for the end-Ordovician glaciation. Nature Communications 5, 4485.

Grahn, Y., Caputo, M.V., 1992. Early Silurian glaciations in Brazil. Palaeogeography, Palaeoclimatology, Palaeoecology 99, 9-15.
Haq, B.U., Schutter, S.R., 2008. A Chronology of Paleozoic Sea-Level Changes. Science 322, 64-68.
Huh, Y., Chan, L.-H., Zhang, L., Edmond, J.M., 1998. Lithium and its isotopes in major world rivers: implications for weathering and the oceanic budget. Geochimica et Cosmochimica Acta 62, 2039-2051.
Jeppsson, L., 1990. An oceanic model for lithological and faunal changes tested on the Silurian record. Journal of the Geological Society 147, 663-674.
Kocken, I.J., Cramwinckel, M.J., Zeebe, R.E., Middelburg, J.J., Sluijs, A., 2019. The 405 kyr and 2.4 Myr eccentricity components in Cenozoic carbon isotope records. Clim. Past 15, 91-104.
Laskar, J., Robutel, P., Joutel, F., Gastineau, M., Correia, A.C.M., Levrard, B., 2004. A long-term numerical solution for the insolation quantities of the Earth. A&A 428, 261-285.
Laurin, J., Meyers, S.R., Uličný, D., Jarvis, I., Sageman, B.B., 2015. Axial obliquity control on the greenhouse carbon budget through middle- to high-latitude reservoirs. Paleoceanography 30, 133-149.
Lechler, M., Pogge von Strandmann, P.A.E., Jenkyns, H.C., Prosser, G., Parente, M., 2015. Lithium-isotope evidence for enhanced silicate weathering during OAE 1a (Early Aptian Selli event). Earth and Planetary Science Letters 432, 210-222.
Lenton, T.M., Crouch, M., Johnson, M., Pires, N., Dolan, L., 2012. First plants cooled the Ordovician. Nature Geoscience 5, 86-89.
Lenton, T.M., Dahl, T.W., Daines, S.J., Mills, B.J.W., Ozaki, K., Saltzman, M.R., Porada, P., 2016. Earliest land plants created modern levels of atmospheric oxygen. Proceedings of the National Academy of Sciences 113, 9704-9709.
Lenton, T.M., Daines, S.J., Mills, B.J.W., 2018. COPSE reloaded: An improved model of biogeochemical cycling over Phanerozoic time. Earth-Science Reviews 178, 1-28.
Loydell, D.K., Frýda, J., 2011. At what stratigraphical level is the mid Ludfordian (Ludlow, Silurian) positive carbon isotope excursion in the type Ludlow area, Shropshire, England. Bulletin of Geosciences 86, 197-208.
McKenzie, N.R., Horton, B.K., Loomis, S.E., Stockli, D.F., Planavsky, N.J., Lee, C.-T.A., 2016. Continental arc volcanism as the principal driver of icehouse-greenhouse variability. Science 352, 444-447.
Melchin, M.J., Mitchell, C.E., Holmden, C., Štorch, P., 2013. Environmental changes in the Late Ordovician–early Silurian: Review and new insights from black shales and nitrogen isotopes. GSA Bulletin 125, 1635-1670.
Misra, S., Froelich, P.N., 2012. Lithium Isotope History of Cenozoic Seawater: Changes in Silicate Weathering and Reverse Weathering. Science 335, 818.
Munnecke, A., Calner, M., Harper, D.A.T., Servais, T., 2010. Ordovician and Silurian sea–water chemistry, sea level, and climate: A synopsis. Palaeogeography, Palaeoclimatology, Palaeoecology 296, 389-413.
Munnecke, A., Samtleben, C., Bickert, T., 2003. The Ireviken Event in the lower Silurian of Gotland, Sweden – relation to similar Palaeozoic and Proterozoic events. Palaeogeography, Palaeoclimatology, Palaeoecology 195, 99-124.
Nardin, E., Goddéris, Y., Donnadieu, Y., Hir, G.L., Blakey, R.C., Pucéat, E., Aretz, M., 2011. Modeling the early Paleozoic long-term climatic trend. GSA Bulletin 123, 1181-1192.
Nowell, G., Luguet, A., Pearson, D., Horstwood, M., 2008. Precise and accurate 186 Os/188 Os and 187 Os/188 Os measurements by multi-collector plasma ionisation mass spectrometry (MC-ICP-MS) part I: Solution analyses. Chemical Geology 248, 363-393.

Page, A., Zalasiewicz, J., Williams, M., Popov, L., 2007. Were transgressive black shales a negative feedback modulating glacioeustasy in the Early Palaeozoic Icehouse. Page 123-156 . Special Publication of the Geological Society of London, The Micropalaeontological Society.
Peucker-Ehrenbrink, B., Ravizza, G., 2000. The marine osmium isotope record. Terra Nova 12, 205-219.
Pogge von Strandmann, P.A., Desrochers, A., Murphy, M., Finlay, A., Selby, D., Lenton, T., 2017. Global climate stabilisation by chemical weathering during the Hirnantian glaciation. Geochemical Perspectives Letters 3, 230-237.
Pogge von Strandmann, P.A.E., Jenkyns, H.C., Woodfine, R.G., 2013. Lithium isotope evidence for enhanced weathering during Oceanic Anoxic Event 2. Nature Geoscience 6, 668-672.
Pogge von Strandmann, P.A.E., Schmidt, D.N., Planavsky, N.J., Wei, G., Todd, C.L., Baumann, K.-H., 2019. Assessing bulk carbonates as archives for seawater Li isotope ratios. Chemical Geology 530, 119338.
Pohl, A., Donnadieu, Y., Le Hir, G., Ferreira, D., 2017. The climatic significance of Late Ordovician‐early Silurian black shales. Paleoceanography 32, 397-423.
Pohl, A., Donnadieu, Y., Le Hir, G., Ladant, J.-B., Dumas, C., Alvarez-Solas, J., Vandenbroucke, T.R.A., 2016. Glacial onset predated Late Ordovician climate cooling. Paleoceanography 31, 800-821.
Rasmussen, C.M.Ø., Kröger, B., Nielsen, M.L., Colmenar, J., 2019. Cascading trend of Early Paleozoic marine radiations paused by Late Ordovician extinctions. Proceedings of the National Academy of Sciences 116, 7207.
Sauzéat, L., Rudnick, R.L., Chauvel, C., Garçon, M., Tang, M., 2015. New perspectives on the Li isotopic composition of the upper continental crust and its weathering signature. Earth and Planetary Science Letters 428, 181-192.
Scotese, C., 2016. PALEOMAP PaleoAtlas for GPlates and the PaleoData Plotter Program, PALEOMAP Project. See http://www.earthbyte.org/paleomap-paleoatlas-for-gplates (accessed 1st October 2019).
Selby, D., Creaser, R.A., 2003. Re–Os geochronology of organic rich sediments: an evaluation of organic matter analysis methods. Chemical Geology 200, 225-240.
Smoliar, M.I., Walker, R.J., Morgan, J.W., 1996. Re-Os Ages of Group IIA, IIIA, IVA, and IVB Iron Meteorites. Science 271, 1099-1102.
Sproson, A.D., 2020. Pacing of the latest Ordovician and Silurian carbon cycle by a ~4.5 Myr orbital cycle. Palaeogeography, Palaeoclimatology, Palaeoecology 540, 109543.
Stockey, R.G., Cole, D.B., Planavsky, N.J., Loydell, D.K., Frýda, J., Sperling, E.A., 2020. Persistent global marine euxinia in the early Silurian. Nature Communications 11, 1804.
Sutcliffe, O.E., Dowdeswell, J.A., Whittington, R.J., Theron, J.N., Craig, J., 2000. Calibrating the Late Ordovician glaciation and mass extinction by the eccentricity cycles of Earth's orbit. Geology 28, 967-970.
Trotter, J.A., Williams, I.S., Barnes, C.R., Lécuyer, C., Nicoll, R.S., 2008. Did Cooling Oceans Trigger Ordovician Biodiversification? Evidence from Conodont Thermometry. Science 321, 550-554.
Trotter, J.A., Williams, I.S., Barnes, C.R., Männik, P., Simpson, A., 2016. New conodont δ18O records of Silurian climate change: Implications for environmental and biological events. Palaeogeography, Palaeoclimatology, Palaeoecology 443, 34-48.

Supplementary Material

Title

Osmium and lithium isotope evidence for weathering feedbacks linked to orbitally paced organic carbon burial and Silurian glaciations

Authors

Adam D. Sproson [a, b, *], Philip A. E. Pogge von Strandmann [c, d], David Selby [a, e], Emilia Jarochowska [f], Jiří Frýda [g, h], Jindřich Hladil [i], David K. Loydell [j], Ladislav Slavík [i], Mikael Calner [k], Georg Maier [f], Axel Munnecke [f], Timothy M. Lenton [l]

Affiliations

[a] Department of Earth Sciences, Durham University, Science Labs, Durham, DH1 3LE, UK.

[b] Biogeochemistry Research Center, Japan Agency for Marine-Earth Science and Technology, Yokosuka, Kanagawa 237-0061, Japan

[c] LOGIC, Institute of Earth and Planetary Sciences, University College London and Birkbeck, University of London, Gower Street, London, WC1E 6BT, UK.

[d] Institute of Geosciences, Johannes Gutenberg University, 55122 Mainz, Germany.

[e] State Key Laboratory of Geological Processes and Mineral Resources, School of Earth Resources, China University of Geosciences, Wuhan, 430074, Hubei, China.

[f] GeoZentrum Nordbayern, Friedrich-Alexander-Universität Erlangen-Nürnberg, Loewenichstraße 28, 91054 Erlangen, Germany

[g] Czech University of Life Sciences, Faculty of Environmental Sciences, Kamýcká 961/129, 165 21 Praha 6-Suchdol, Czech Republic.
[h] Czech Geological Survey, Klárov 3, 11821 Prague1, Czech Republic

[i] Institute of Geology of the Czech Academy of Sciences, Prague, Czech Republic

[j] School of the Environment, Geography and Geosciences, University of Portsmouth, Burnaby Road, Portsmouth PO1 3QL, UK.

[k] Department of Geology, Lund University, Sölvegatan 12, 223 62 Lund, Sweden.

[l] Global Systems Institute, University of Exeter, Laver Building (Level 8), North Park Road, Exeter, EX4 4QE, UK.
*corresponding author (adamsproson@gmail.com; sprosona@jamstec.go.jp)

Contents

1. Geological Setting

In this study, four shale sections were analysed for osmium isotopes and three bulk carbonate sections were analysed for lithium isotopes. Combined, these sections cover four intervals of

Silurian time: the late Telychian to early Sheinwoodian; mid Homerian; mid-Ludfordian; and the Silurian-Devonian boundary. Shales from the Aizpute-41 core (Latvia) and carbonates from the Lusklint and Lickershamn (Gotland, Sweden) sections cover the latest Telychian to earliest Sheinwoodian. Shales from the Bartoszyce core (Poland) and bulk carbonates from the Hunninge-1 core (Gotland, Sweden) cover the mid Homerian. Shales and bulk carbonates from the Kosov (Czech Republic) section cover the mid-Ludfordian. Finally, shales from the Klonk core (Czech Republic) cover the Silurian-Devonian Boundary for Os isotope analysis only. The following will detail the geology, sampling strategy and paleoenvironment of each section studied.

1.1 Aizpute-41 core

The Aizpute-41 core, which provided late Telychian-early Sheinwoodian samples for this study, was drilled in the town of Aizpute, situated in western Latvia, in the deeper shelf part of the Eastern Baltoscandian Basin. The latest Llandovery (Telychian) beds consist of greenish and brownish grey marlstones, whereas the lowermost Wenlock (lower Sheinwoodian) consists of green, grey and brown marlstones with calcareous marlstones (Loydell et al., 2003). In the Telychian, darker graptolitic shales are interbedded with paler, non-graptolitic strata. The lower Sheinwoodian of the core is graptolitic throughout. The sampling strategy of graptolite-rich, relatively high total organic carbon (TOC) shales was followed according to Loydell et al. (2003). The $\delta^{13}C_{carb}$ data for the drill core material are reported by Cramer et al. (2010).

1.2 Lusklint and Lickershamn

The late Telychian-early Sheinwoodian Lower Visby Formation (LVF) and the early Sheinwoodian Upper Visby Formation (UVF) is exposed at Lusklint and Lickershamn along the north-western coast of Gotland, Sweden. The LVF consists of up to 12 m of regular limestone-marl alternations, typically, of 2-5 cm thick, wavy bedded to nodular argillaceous limestones interbedded with approximately 10 cm thick marls. The unit was deposited in a distal shelf environment, below storm wave base (Calner et al., 2004; Munnecke et al., 2003). The bedding in the UVF is not as regular as in the underlying LVF and shows a general upward increase in bioclastic limestone and decrease in the thickness of interbedded marls. This is due to a relative and successive shallowing of depositional environment. Samples from the LVF were sampled from Lusklint whereas samples from the UVF were sampled from Lickershamn. The $\delta^{13}C_{carb}$ data for the samples are reported by Maier (2010).

1.3 Bartoszyce

The mid-Homerian Bartoszyce IG 1 borehole is in the eastern part of the Peribaltic Syneclize of the Polish part of the East European platform. The core consists of sparsely bioturbated, light-grey laminated and calcareous mudstones (Porębska et al., 2004). The sampling strategy of relatively high TOC shales, $\delta^{13}C_{carb}$ and $\delta^{18}O_{carb}$ data are reported in Porębska et al. (2004).

1.4 Hunninge-1 core

The mid-Homerian Hunninge-1 core was drilled in the Hunninge quarry near Klintehamn on western Gotland, Sweden (See Calner et al. (2006) for a full description). The core includes, in ascending order, the Slite Marl, the Fröjel Formation (including the Svarvare and Gannarve members), the Halla Formation (including the Bara, Mulde Brick-clay, and Djupvik members), and the lowermost portion of the Klinteberg Formation. The Gannarve, Bara, Mulde Brick-clay, and Djupvik members were sampled for lithium isotopes for this study. The Gannarve Member consists of alternating beds of brownish, argillaceous, dolomitic siltstone with silty, dolomitic marlstone, together representing alternating storm-

and fair-weather deposition (Calner et al., 2006). The Bara Oolite Member is separated from the Gannarve Member by an erosional unconformity in more proximal areas. The Hunninge-1 core was drilled at the feather edge of the unconformity and although an erosional surface is noted at the top of the Gannarve Member, this surface does not appear to be associated with any hiatus based on biostratigraphy and/or carbon isotope stratigraphy (Calner et al., 2006). The Bara Oolite Member in this area is a thin limestone with coated grains. The Mulde Brick-clay Member consists of dense mudstone and calcareous mudstone alternating with argillaceous limestone bands or nodules. The overlying Djupvik Member is similarly a limestone-marl alternation but shows a higher limestone-marl ratio (Calner et al., 2006). The sampling strategy for carbonates and $\delta^{13}C_{carb}$ data is presented in Calner et al. (2006).

1.5 Kosov

The mid-Ludfordian Kosov section is in the Barrandian region of the Czech Republic. The *Neocucullograptus kozlowskii* Biozone consists of alternating beds of grey finely laminated shale and light grey packstones and grainstones, while the overlying *Pristiograptus dubius postfrequens* Biozone consists of alternating beds of light grey packstones/grainstones and mudstones or grey coarsely laminated calcareous shales. The sampling strategy of carbonates and relatively high TOC shales and $\delta^{13}C_{carb}$ data is published in Frýda and Manda (2013).

1.6 Klonk core

The Přídolí-Lochkovian (Silurian-Devonian) GSSP is in the Czech Republic 35 km southwest of Prague. The latest Přídolí and earliest Lochkovian beds consist of greyish-black, platy, mostly fine-grained bituminous limestones alternating with calcareous shale interbeds with occasional stringers of crinoidal limestones (Slavík and Hladil, 2019). The sampling strategy of relatively high total organic carbon (TOC) drill core material was followed according to Crick et al. (2001). The $\delta^{13}C_{carb}$ and $\delta^{18}O_{carb}$ data for the drill core material is reported by Buggisch and Mann (2004).

2. Supplementary Results

2.1 Rhenium-osmium isotope data

Rhenium and osmium isotope compositions and abundance data for the Aizpute-41 (Latvia), Bartoszyce (Poland), Kosov (Czech Republic) and Klonk (Czech Republic) samples are presented in Table S1.

Table S1. Rhenium and osmium abundance and isotope data for the Aizpute-41, Bartoszyce, Kosov and Klonk shale samples. Initial $^{187}Os/^{188}Os$ ($^{187}Os/^{188}Os_i$) were calculated using graptolite biozone ages (Melchin et al., 2012).

Depth (m)	Re (ppb)	2 s.e.	Os (ppt)	2 s.e.	$^{187}Re/^{188}Os$	2 s.e.	$^{187}Os/^{188}Os$	2 s.e.	$^{187}Os/^{188}Os_i$	2 s.e.
Aizpute-41 Core, Latvia										
910.06	2.22	0.01	65.0	0.7	206.9	2.9	2.10	0.04	0.602	0.015
910.19	2.31	0.01	67.2	0.7	208.8	3.0	2.11	0.04	0.595	0.014
910.60	2.42	0.01	74.0	0.8	196.9	2.8	2.06	0.04	0.629	0.015
910.90	2.91	0.05	73.8	0.6	244.6	4.9	2.33	0.03	0.558	0.013
911.33	3.23	0.03	87.2	0.7	226.6	3.0	2.18	0.03	0.540	0.010
912.00	2.79	0.05	77.3	0.6	217.4	4.3	2.04	0.03	0.466	0.011
912.90	2.17	0.04	98.9	0.5	121.7	2.3	1.30	0.01	0.414	0.008
914.01	2.02	0.15	84.9	0.5	136.6	10.1	1.59	0.01	0.602	0.045

914.74	5.60	0.01	130.7	1.1	271.3	2.5	2.53	0.03	0.564	0.009
914.80	5.53	0.02	135.4	1.1	250.0	2.3	2.20	0.03	0.391	0.006
914.95	3.26	0.01	115.1	0.7	166.7	1.2	1.83	0.02	0.620	0.007
915.90	7.88	0.25	128.0	0.9	433.6	14.0	3.66	0.03	0.521	0.017
916.50	10.52	0.19	152.8	1.0	502.4	9.2	4.06	0.03	0.422	0.008
917.70	10.20	0.33	144.1	1.1	525.5	17.0	4.28	0.03	0.468	0.016
919.96	9.59	0.17	144.5	1.1	481.5	8.9	4.00	0.03	0.515	0.010
924.70	1.88	0.01	81.2	0.5	131.7	1.1	1.51	0.01	0.557	0.007
924.98	1.52	0.01	78.6	0.5	108.2	0.8	1.38	0.01	0.593	0.007
925.21	3.77	0.04	98.3	0.5	237.6	2.6	2.32	0.01	0.597	0.007
925.65	9.64	0.03	152.7	1.3	460.6	3.5	4.07	0.04	0.733	0.009
928.01	16.74	0.04	207.6	1.8	644.7	4.5	5.18	0.05	0.511	0.006
930.38	17.95	0.32	230.0	1.8	606.8	11.2	4.83	0.04	0.433	0.009
932.35	27.46	0.07	274.0	2.2	929.8	5.2	7.23	0.05	0.489	0.004
934.20	15.86	0.04	249.7	1.9	439.6	2.9	3.47	0.03	0.287	0.003
935.82	5.98	0.02	143.5	0.9	253.5	1.7	2.13	0.02	0.296	0.003
Bartoszyce Core, Poland										
1674.20	12.46	0.22	162.3	1.3	597.0	11.1	4.83	0.04	0.551	0.011
1672.90	12.55	0.40	196.3	1.5	454.8	14.8	3.78	0.03	0.517	0.017
1670.00	8.71	0.02	131.5	1.0	482.9	3.0	4.06	0.03	0.595	0.006
1666.65	9.46	0.17	147.8	1.0	461.5	8.5	3.93	0.03	0.618	0.012
1665.00	14.96	0.27	238.4	1.6	449.5	8.3	3.86	0.03	0.638	0.013
1663.75	3.01	0.05	69.8	0.6	275.5	5.5	2.65	0.03	0.670	0.016
1662.30	1.71	0.06	42.7	0.5	253.2	8.9	2.53	0.05	0.711	0.029
1661.80	1.10	0.02	27.9	0.4	244.2	6.7	2.35	0.07	0.603	0.024
1661.70	1.29	0.01	30.0	0.4	268.5	5.7	2.44	0.07	0.513	0.018
1661.40	1.17	0.02	34.6	0.5	203.6	5.6	2.04	0.06	0.580	0.023
1660.72	0.74	0.02	26.2	0.6	166.2	8.7	1.76	0.10	0.567	0.044
1660.70	0.51	0.01	34.2	0.7	81.1	3.4	1.18	0.07	0.594	0.042
1660.00	4.09	0.04	87.4	2.1	298.5	12.4	2.61	0.15	0.471	0.033
1659.75	3.80	0.07	106.3	0.9	221.5	4.4	2.32	0.03	0.727	0.017
1659.65	0.53	0.01	39.8	0.2	72.9	1.1	1.16	0.01	0.639	0.012
1657.95	3.81	0.01	126.9	1.0	177.5	1.5	1.87	0.02	0.601	0.009
1656.72	4.38	0.25	126.4	0.9	210.1	12.1	2.12	0.02	0.611	0.036
1652.36	8.61	0.49	192.2	1.2	283.8	16.3	2.54	0.02	0.500	0.029
1648.20	7.93	0.02	184.6	1.3	272.9	2.0	2.57	0.02	0.615	0.007
1647.20	9.32	0.02	204.1	1.2	290.9	1.5	2.60	0.02	0.515	0.004
Kosov, Czech Republic										
-7.60	5.60	0.39	79.7	1.0	499.9	35.7	3.78	0.07	0.235	0.017
-6.5	3.28	0.01	55.9	0.6	401.1	4.9	3.33	0.05	0.486	0.010
-6	4.26	0.01	60.9	0.7	518.7	6.1	4.25	0.07	0.570	0.011
-5.00	4.45	0.08	100.9	0.8	285.9	5.8	2.79	0.03	0.761	0.017
-3.65	9.34	0.53	134.0	1.0	511.4	29.4	4.13	0.03	0.509	0.029
-2.20	2.07	0.04	22.3	0.3	802.9	19.5	6.25	0.13	0.559	0.018
-1.00	8.35	0.16	102.7	1.1	623.6	12.8	4.66	0.06	0.243	0.006

-0.15	15.28	0.87	145.7	1.4	949.4	54.7	6.86	0.06	0.129	0.008
0.15	1.65	0.01	25.1	0.2	473.3	5.9	3.89	0.05	0.533	0.009
1.75	0.33	0.03	12.9	0.1	146.1	11.7	1.48	0.03	0.443	0.036
2.10	0.84	0.02	30.0	0.5	160.7	5.4	1.61	0.06	0.472	0.024
4.25	0.22	0.00	10.4	0.1	124.8	3.1	1.63	0.04	0.740	0.024
9.45	0.64	0.04	27.0	0.6	140.7	10.0	1.93	0.11	0.930	0.085
14.60	1.16	0.00	21.9	0.3	355.3	7.6	3.12	0.09	0.605	0.022
16.60	3.02	0.01	35.4	0.4	721.7	7.2	5.90	0.08	0.788	0.013
Klonk Core, Czech Republic										
16.37	1.93	0.07	66.3	0.5	175.0	6.4	2.02	0.03	0.789	0.031
17.53	2.77	0.01	81.6	1.1	206.7	4.3	2.13	0.06	0.682	0.024
18.67	7.30	0.26	176.3	1.5	259.9	9.5	2.44	0.03	0.619	0.024
19.82	4.45	0.16	152.2	1.2	172.9	6.3	1.87	0.02	0.662	0.026
20.73	2.60	0.01	137.6	1.4	110.7	1.6	1.78	0.03	1.006	0.024
21.22	1.98	0.01	104.8	1.1	110.6	1.6	1.76	0.03	0.984	0.024
22.25	2.37	0.01	111.1	1.1	126.8	1.8	1.93	0.04	1.044	0.025
23.27	1.81	0.01	64.0	0.7	176.5	2.7	2.39	0.05	1.149	0.029
23.45	3.50	0.01	76.4	1.1	304.0	5.8	3.03	0.08	0.898	0.030
23.65	6.46	0.02	148.2	1.9	282.7	4.7	2.77	0.06	0.792	0.022
23.95	2.35	0.01	59.6	0.7	248.2	4.3	2.48	0.06	0.745	0.021
24.25	4.61	0.02	142.2	1.7	198.0	3.3	2.17	0.05	0.787	0.022
24.4	6.00	0.02	158.1	1.9	234.3	4.0	2.29	0.05	0.643	0.019
24.54	8.84	0.03	182.4	1.6	321.0	3.2	3.00	0.04	0.750	0.012
24.65	3.52	0.02	124.9	1.5	167.0	3.0	1.88	0.04	0.710	0.021
24.72	3.76	0.02	125.2	1.5	181.9	3.2	2.11	0.05	0.832	0.024
24.77	4.07	0.02	161.2	1.8	146.6	2.5	1.70	0.04	0.671	0.019
24.87	5.77	0.02	150.2	1.8	235.5	4.1	2.22	0.05	0.567	0.016
24.87	6.04	0.02	159.7	1.3	232.2	2.1	2.22	0.03	0.590	0.009
25.01	3.12	0.02	84.5	1.1	229.3	4.4	2.33	0.06	0.721	0.022
25.21	5.06	0.02	123.4	1.6	258.1	4.6	2.47	0.06	0.665	0.020
25.35	6.71	0.02	136.2	1.8	325.3	5.7	2.97	0.07	0.691	0.020
25.42	2.54	0.01	111.1	1.2	137.3	2.0	2.00	0.04	1.039	0.025
25.60	6.34	0.02	116.8	1.4	370.3	5.3	3.32	0.07	0.725	0.018
25.98	3.75	0.01	118.8	1.3	190.5	2.7	2.07	0.04	0.732	0.018
26.22	2.13	0.01	99.4	1.0	123.5	1.8	1.62	0.03	0.754	0.018
26.45	5.13	0.02	152.4	1.3	215.9	2.0	2.66	0.03	1.148	0.017
26.78	10.42	0.04	175.5	2.4	411.3	6.9	3.48	0.08	0.602	0.017
27.25	6.47	0.02	208.0	2.4	186.2	3.1	1.98	0.04	0.673	0.019
27.8	17.46	0.06	200.9	1.4	729.0	3.9	5.81	0.03	0.697	0.005
28.34	4.55	0.02	105.6	0.9	274.3	2.6	2.60	0.03	0.678	0.010
29.28	6.86	0.24	185.3	1.0	229.0	8.2	2.30	0.01	0.690	0.025
30.15	9.95	0.35	224.8	1.3	283.7	10.1	2.65	0.02	0.665	0.024
31.45	6.94	0.25	206.0	1.1	204.8	7.3	2.14	0.01	0.701	0.025

2.1.1 Aizpute-41 Core

The Re and Os abundances and $^{187}Re/^{188}Os$ and $^{187}Os/^{188}Os$ ratios are variable throughout the Aizpute-41 section ([Re] = 1.52 to 27.46 ppb; [Os] = 65 to 274 ppt; $^{187}Re/^{188}Os$ = 108 to 930; $^{187}Os/^{188}Os$ = 1.3 to 7.2; Table S1). Initial $^{187}Os/^{188}Os$ values range from 0.29 to 0.73 (Table S1; Fig. S1). From 934.2 to 932.35 m, within the uppermost part of the lower *Cyrtograptus lapworthi* and lowermost *C. murchisoni* Biozones, $^{187}Os/^{188}Os_i$ increases from ~0.29 to ~0.73. From 925.65 to 916.5 m, $^{187}Os/^{188}Os_i$ decreases from ~0.73 to ~0.42. The $^{187}Os/^{188}Os_i$ then fluctuates between ~0.39 and ~0.62 within the upper part of the *murchisoni* Biozone. From 912.9 to 910.6 m, spanning the *Monograptus firmus* to lowermost *M. riccartonensis* Biozone, the $^{187}Os/^{188}Os_i$ increases from 0.41 to 0.63. The top of the cored interval is within the lower *riccartonensis* Biozone and this prevents further analysis into the Wenlock.

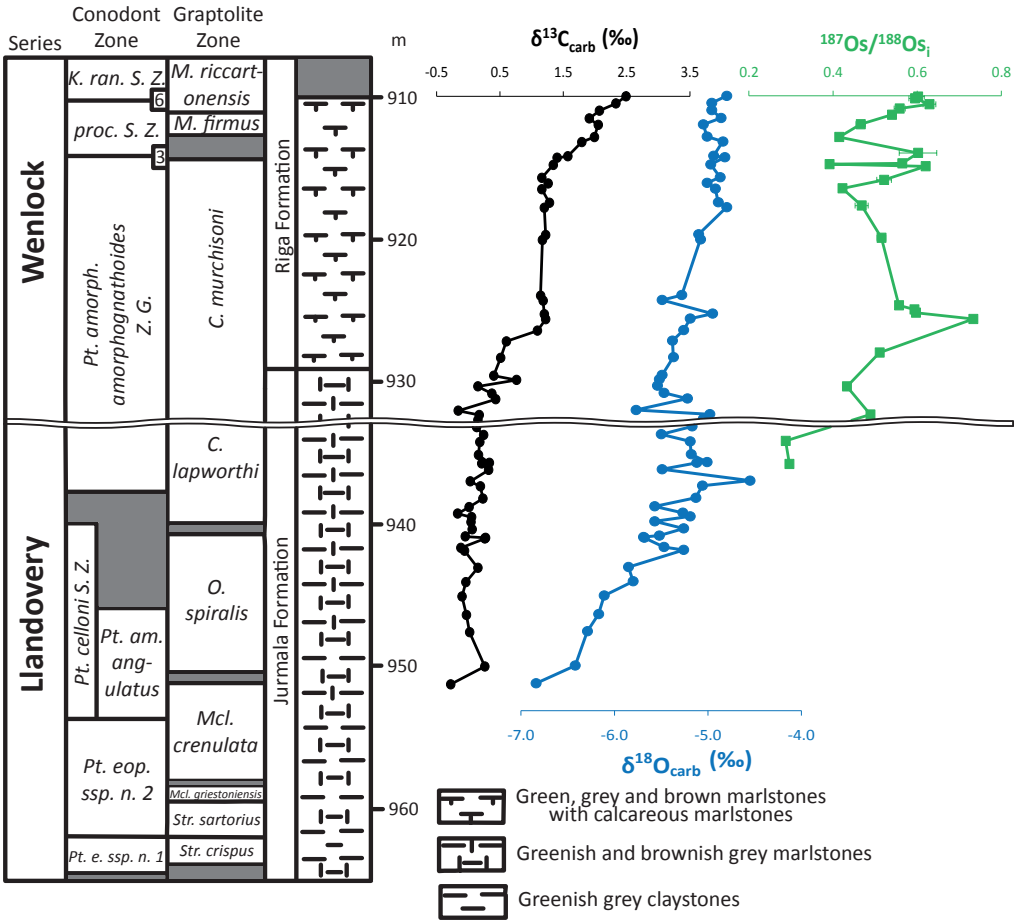

Fig. S1. Osmium ($^{187}Os/^{188}Os_i$, green squares), oxygen ($\delta^{18}O_{carb}$, blue circles) and carbon ($\delta^{13}C_{carb}$, black circles) isotope ratios for shales and carbonates from the Llandovery to Wenlock Aizpute-41 core. Biozone, lithology and carbon and oxygen isotope data have been adapted from Cramer *et al*. (2010). See text for details.

2.1.2 Bartoszyce Core

The Re and Os abundances and $^{187}Re/^{188}Os$ and $^{187}Os/^{188}Os$ ratios are variable throughout the Bartoszyce IG-1 core ([Re] = 0.5 to 15 ppb; [Os] = 26.2 to 238.4 ppt; $^{187}Re/^{188}Os$ = 73 to 597; $^{187}Os/^{188}Os$ = 1.2 to 4.8; Table S1). Initial $^{187}Os/^{188}Os$ values range from 0.47 to 0.73 (Table S1; Fig. S2). From 1672.9 to 1662.3 m, from the uppermost *Cyrtograptus lundgreni* to the base of the *Gothograptus nassa* Biozone, the $^{187}Os/^{188}Os_i$ increases from ~0.52 to ~0.71. Immediately afterwards, the $^{187}Os/^{188}Os_i$ decreases from ~0.71 to ~0.51 where it remains relatively low (~0.5) between 1661.7 to 1660 m. From 1660 to 1659.7 m, the $^{187}Os/^{188}Os_i$

sharply increases from ~0.47 to ~0.73. The $^{187}Os/^{188}Os_i$ then proceeds to decrease throughout the rest of the *nassa* Biozone.

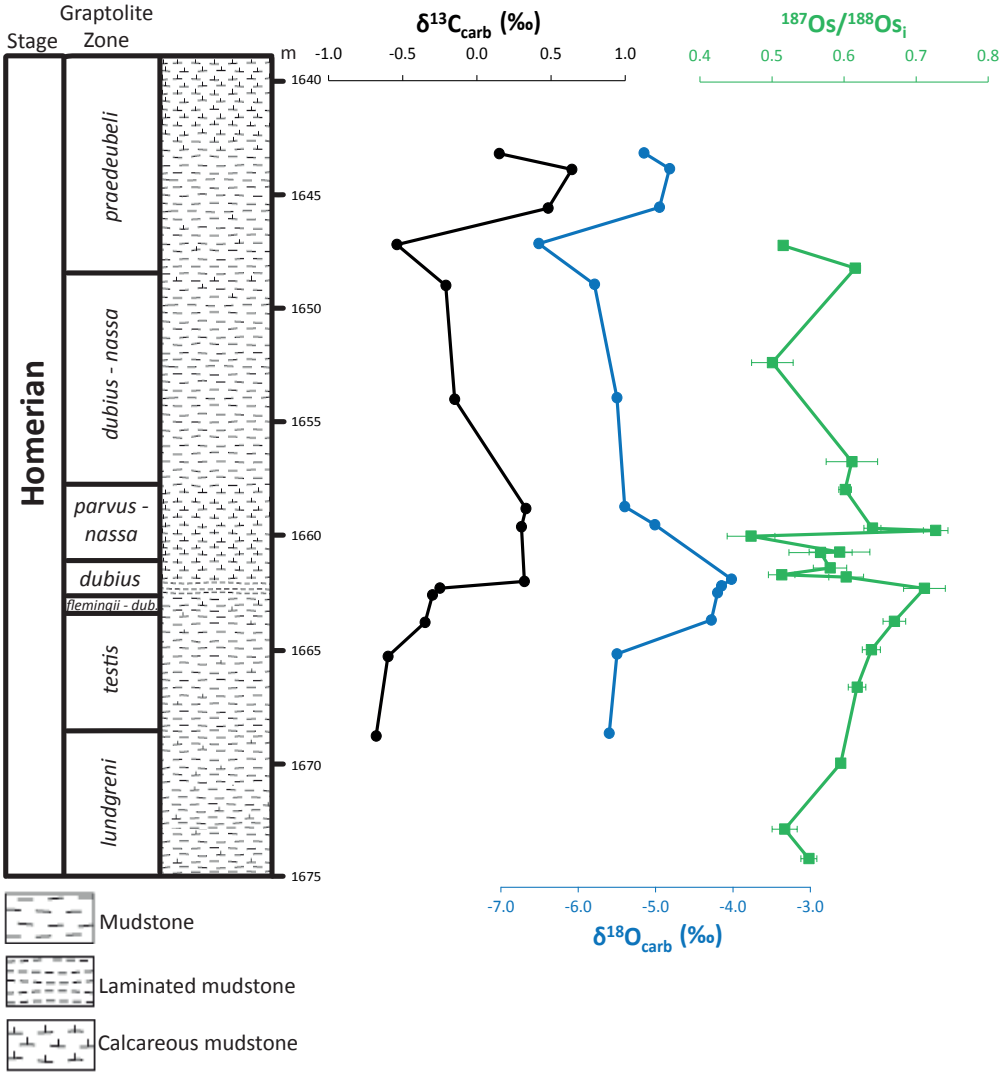

Fig. S2. Osmium ($^{187}Os/^{188}Os_i$, green squares), oxygen ($\delta^{18}O_{carb}$, blue circles) and carbon ($\delta^{13}C_{carb}$, black circles) isotope ratios for shales and carbonates from the Homerian Bartoszyce section. Biozone, lithology and carbon and oxygen isotope data have been adapted from Porębska *et al.* (2004). See text for details.

2.1.3 Kosov section

The Re and Os abundances and $^{187}Re/^{188}Os$ and $^{187}Os/^{188}Os$ ratios are variable throughout the Kosov section ([Re] = 0.2 to 15.3 ppb; [Os] = 10.4 to 145.7 ppt; $^{187}Re/^{188}Os$ = 124.8 to 949.4; $^{187}Os/^{188}Os$ = 1.5 to 6.9; Table S1). Initial $^{187}Os/^{188}Os$ values range from 0.13 to 0.93 (Table S1; Fig. S3). From -7.6 to -5 m, the $^{187}Os/^{188}Os_i$ increases from ~0.23 to ~0.76. Prior to the base of the *Pristiograptus dubius postfrequens* Biozone, the $^{187}Os/^{188}Os_i$ decreases from ~0.76 to ~0.13 between -5 and -0.13 m. The $^{187}Os/^{188}Os_i$ then increases from ~0.13 to ~0.93 between 0.13 and 9.45 m before decreasing again towards the end of the *dubius postfrequens* Biozone.

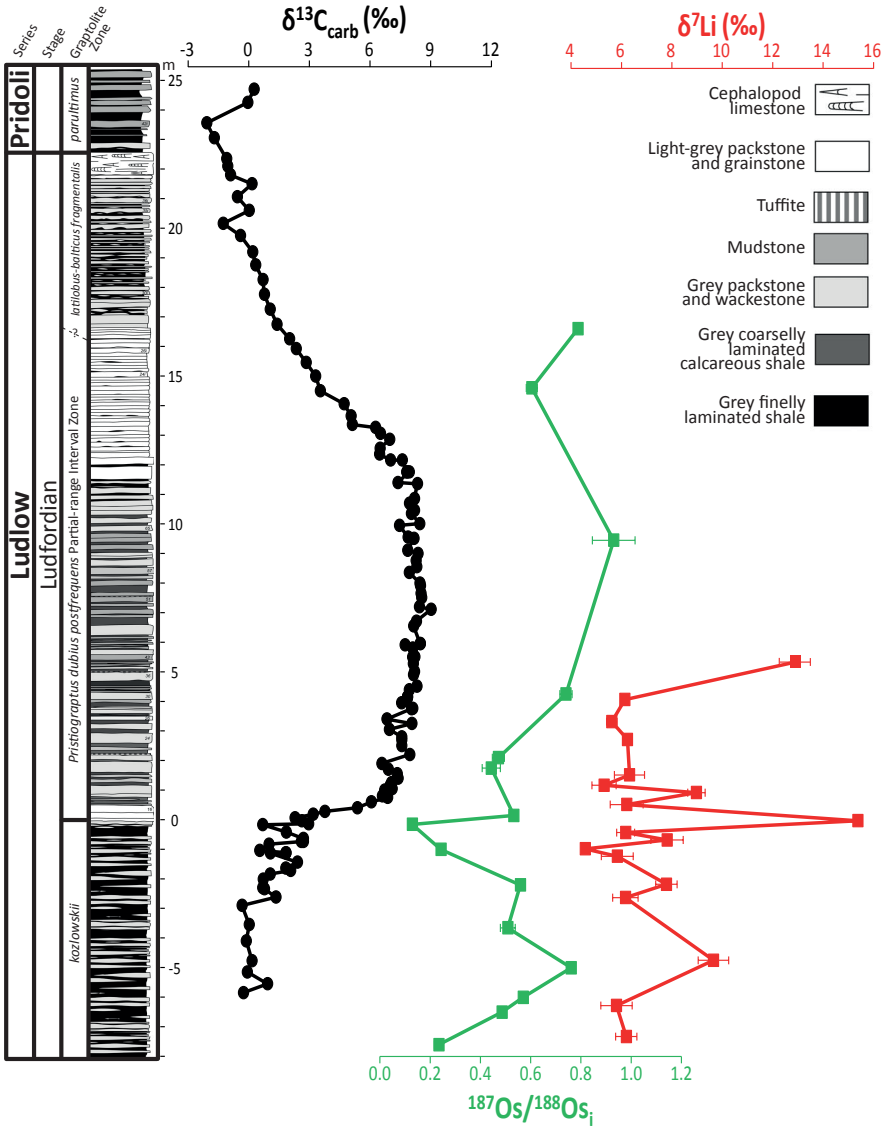

Fig. S3. Osmium ($^{187}Os/^{188}Os_i$, green squares), Lithium (δ^7Li, red squares) and carbon ($\delta^{13}C_{carb}$, black circles) isotope ratios for carbonates and shales from the Ludfordian Kosov section. Biozone, lithology and carbon isotope data have been adapted from Frýda and Manda (2013). See text for details.

2.1.4 Klonk core

The Re and Os abundances and $^{187}Re/^{188}Os$ and $^{187}Os/^{188}Os$ ratios are variable throughout the Klonk core ([Re] = 1.8 to 17.4 ppb; [Os] = 59.6 to 224.8 ppt; $^{187}Re/^{188}Os$ = 110 to 729; $^{187}Os/^{188}Os$ = 1.6 to 5.8; Table S1). Initial $^{187}Os/^{188}Os$ values range from 0.57 to 1.15 (Table S1; Fig. S4). From 31.45 to 26.78 m, the $^{187}Os/^{188}Os_i$ are moderately radiogenic, ranging from ~0.6 to ~0.7. Between 26.78 and 25.35 m, the $^{187}Os/^{188}Os_i$ fluctuates between ~0.6 and ~1.15. Across the Silurian-Devonian boundary, the $^{187}Os/^{188}Os_i$ is also moderately radiogenic, with values between ~0.57 and ~0.83 (25.35 to 23.95 m). From 23.95 to 23.27 m, the $^{187}Os/^{188}Os_i$ increases from 0.74 to 1.15 before subsequently decreasing from 1.15 to 0.62 during the lowermost Devonian.

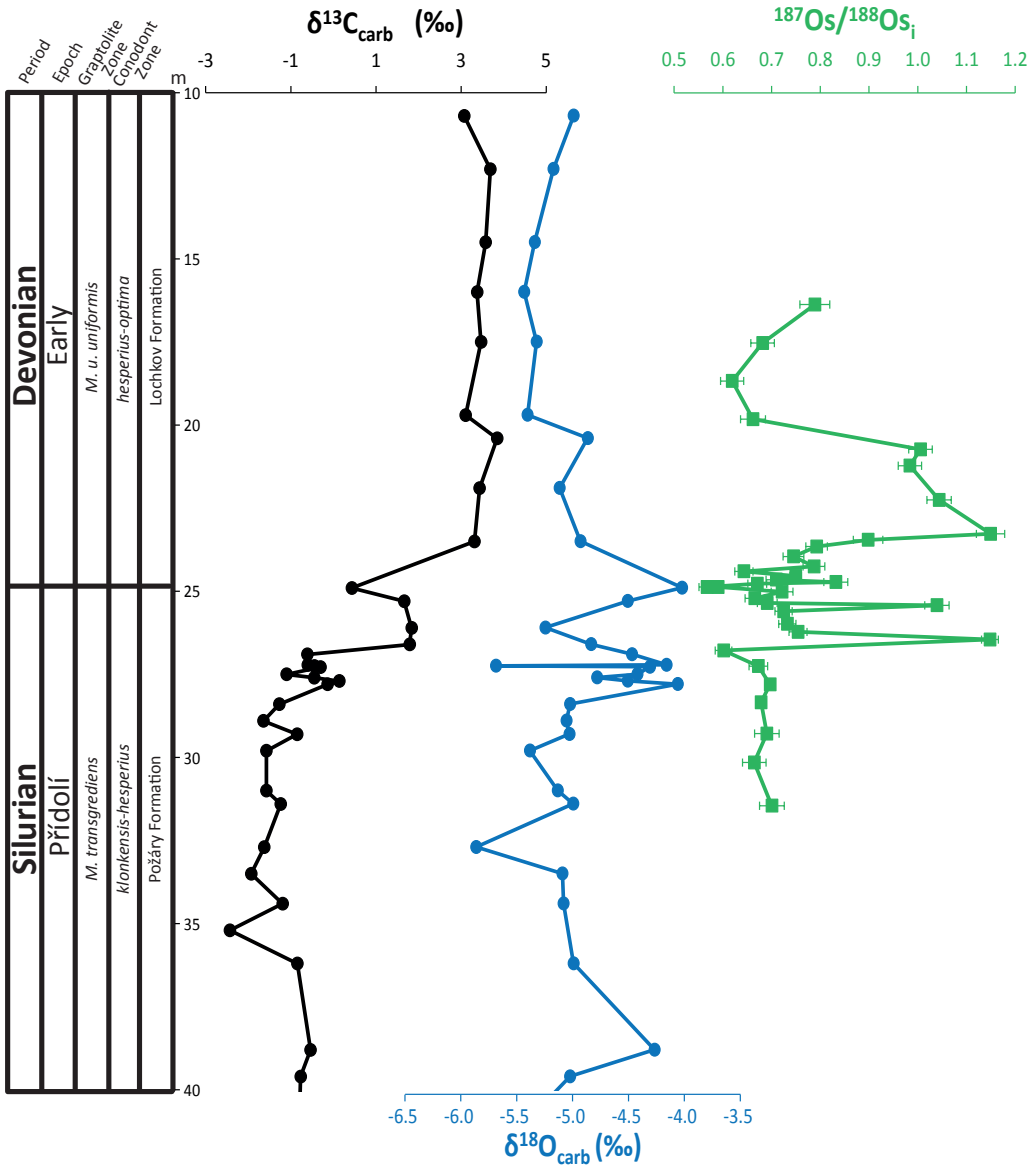

Fig. S4. Osmium ($^{187}Os/^{188}Os_i$, green squares), oxygen ($\delta^{18}O_{carb}$, blue circles) and carbon ($\delta^{13}C_{carb}$, black circles) isotope ratios for carbonates and shales from the Silurian-Devonian GSSP at Klonk. Biozone information adapted from Slavík and Hladil (2019). Carbon and oxygen isotope data have been adapted from Buggisch and Mann (2004). See text for details.

2.2 Lithium isotope and trace metal data

Lithium isotope measurements and trace metal data for the Hunninge-1 (Sweden), Kosov (Czech Republic), Lusklint (Sweden) and Lickershamn (Sweden) samples are presented in Table S2.

Table S2. Lithium isotope and trace metal data for the Hunninge-1, Kosov, Lusklint and Lickershamn carbonate samples.

Depth (m)	δ^7Li (‰)	2 s.d.	Mg/Ca (mmol/mol)	Al/Ca (mmol/mol)	Mn/Ca (mmol/mol)	Sr/Ca (mmol/mol)
Lusklint, Sweden						
7.9	11.0	0.2	6.50	0.27	0.51	0.17

8.7	12.3	0.2	4.81	0.17	0.49	0.09
9.6	11.1	0.3	5.11	0.15	0.45	0.10
10.3	11.6	0.6	4.39	0.12	0.38	0.12
11.3	11.6	0.5	5.53	0.18	0.50	0.18
11.6	11.1	0.8	4.45	0.17	0.47	0.09
Lickershamn, Sweden						
0.19	13.5	0.5	4.00	0.15	0.41	0.09
0.66	12.2	0.1	6.63	0.22	0.38	0.20
1.39	14.7	0.2	67.47	0.60	1.04	1.86
2.25	16.1	0.2	5.36	0.14	0.29	0.22
3.27	17.6	0.5	4.18	0.21	0.22	0.15
4.2	16.1	0.5	4.15	0.08	0.26	0.12
5.8	14.3	0.1	5.15	0.20	0.32	0.17
7.9	16.8	0.5	12.70	0.28	0.92	0.43
11.65	17.9	0.4	9.21	0.51	0.66	0.44
12.4	14.9	0.2	11.65	0.55	0.63	0.43
Hunninge-1 Drillcore, Sweden						
-5.8	10.0	0.5	91.63	0.49	0.97	1.51
-4.4	11.2	0.7	39.32	0.54	2.74	0.75
-2.8	11.4	0.3	28.51	0.29	3.64	0.74
-1.5	11.4	0.5	40.49	1.01	2.46	0.66
-1.1	10.6	0.5	32.11	0.52	1.76	0.29
-0.7	9.9	0.1	20.51	0.12	1.97	0.39
-0.4	12.2	0.2	41.29	0.83	1.89	0.60
-0.2	12.5	0.2	40.12	0.54	1.47	0.68
0.2	12.7	0.3	48.25	1.00	1.07	0.96
0.7	12.6	0.6	24.21	0.11	0.67	0.83
1	13.4	0.3	15.61	0.01	0.50	0.70
1.5	13.8	0.2	19.00	0.01	0.53	0.63
1.8	14.7	0.6	24.94	0.11	0.49	1.27
4.8	13.0	0.7	22.07	bd	0.61	1.35
6.6	13.5	0.3	41.11	0.05	0.96	1.60
9.56	13.8	0.4	36.60	0.33	0.83	1.53
10.5	13.7	0.3	83.28	0.47	1.17	1.98
12.74	13.2	0.4	172.55	0.33	0.97	1.52
13.66	13.9	0.4	185.47	0.41	0.93	1.49
15.05	7.9	0.5	7.09	0.60	0.29	0.42
23.2	12.1	0.7	3.66	0.21	0.15	0.07
Kosov, Czech Republic						
-7.4	6.19	0.4				
-6.3	5.80	0.6				
-4.77	9.6	0.6	13.64	bd	1.23	0.56
-2.65	6.2	0.5	12.69	0.07	0.78	0.55
-2.2	7.8	0.4	14.60	0.01	0.74	0.51
-1.25	5.8	0.6	14.48	0.11	0.85	0.44
-1	4.6	0.1	12.34	0.20	0.85	0.79

-0.7	7.8	0.6				
-0.45	6.2	0.4				
-0.05	15.4	0.2	10.93	0.05	0.47	0.97
0.5	6.2	0.7				
0.9	9.0	0.3	13.24	0.13	0.35	0.95
1.15	5.3	0.5				
1.5	6.3	0.6				
2.7	6.2	0.2				
3.3	5.6	0.2				
4.05	6.1	0.1	13.67	0.07	0.41	0.99
5.28	12.8	0.6	13.29	0.06	0.31	0.98

2.2.1 Lusklint section

The Mg/Ca, Al/Ca, Mn/Ca and Sr/Ca ratios show a narrow range through the Lusklint section (Mg/Ca = 4.4 to 6.5 mmol/mol; Al/Ca = 0.12 to 0.27 mmol/mol; Mn/Ca = 0.38 to 0.51 mmol/mol; Sr/Ca = 0.09 to 0.18 mmol/mol; Table S2). The Al/Ca ratios remain below the ~0.8 mmol/mol threshold, suggesting little influence from Li leached from clays. The δ^7Li values range from 11 to 12.3 ‰ (Table S2; Fig. S5). The δ^7Li values remain relatively constant throughout the *Pseudooneotodus bicornis* and *Pterospathodus pennatus procerus* biozones, with slightly higher values at the boundary between the upper and lower *bicornis* biozones.

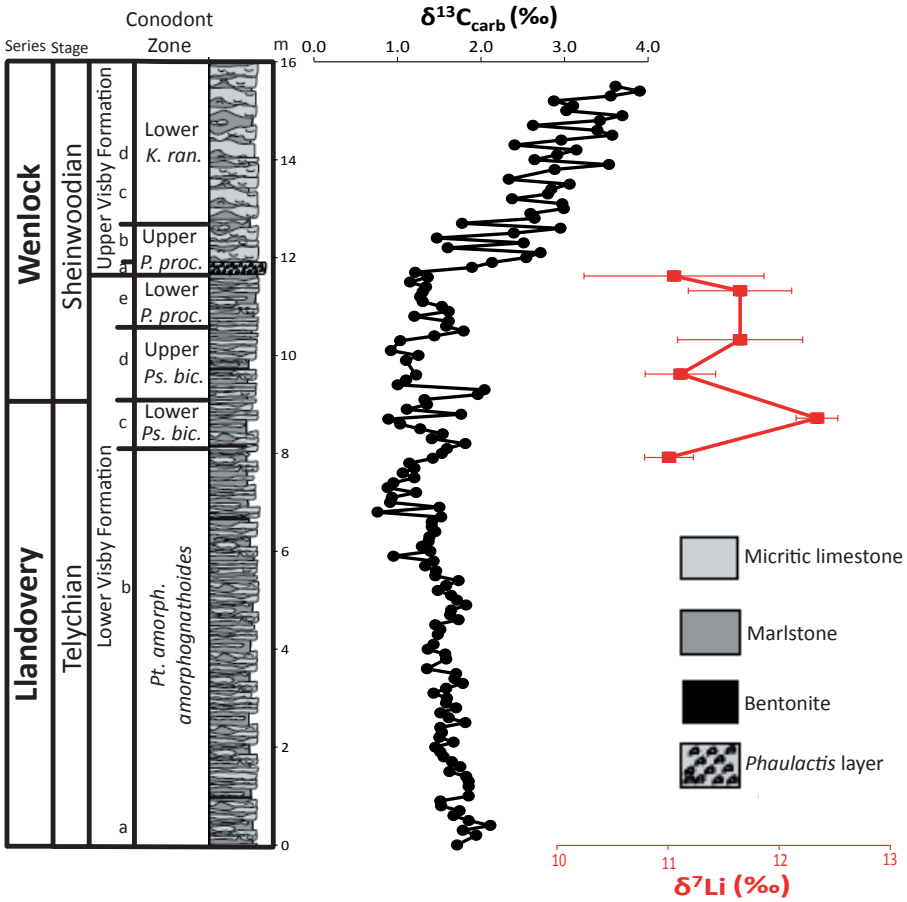

Fig. S5. Lithium (δ^7Li, red squares) and carbon ($\delta^{13}C_{carb}$, black circles) isotope ratios for carbonates from the Llandovery to Wenlock Lusklint section. Biozone, lithology and carbon data have been adapted from Maier (2010). See text for details.

2.2.2 Lickershamn section

The Mg/Ca, Al/Ca, Mn/Ca and Sr/Ca ratios are variable throughout the Lickershamn section (Mg/Ca = 4 to 67.5 mmol/mol; Al/Ca = 0.08 to 0.6 mmol/mol; Mn/Ca = 0.22 to 1.04 mmol/mol; Sr/Ca = 0.09 to 1.86 mmol/mol; Table S2). The Al/Ca ratios remain below the ~0.8 mmol/mol threshold, suggesting little influence from Li leached from clays. The δ^7Li values range from 12.2 to 17.9 ‰ (Table S2; Fig. S6). The δ^7Li values are relatively low (~13 ‰) at the base of the upper *procerus* Biozone before rising to 17.6 ‰ by the end of this Biozone, decreasing again to ~14.3 ‰ during the lower *Kockelella ranuliformis* Biozone. During the upper *ranuliformis* Biozone, δ^7Li values increase again to maximum values of 17.9 ‰.

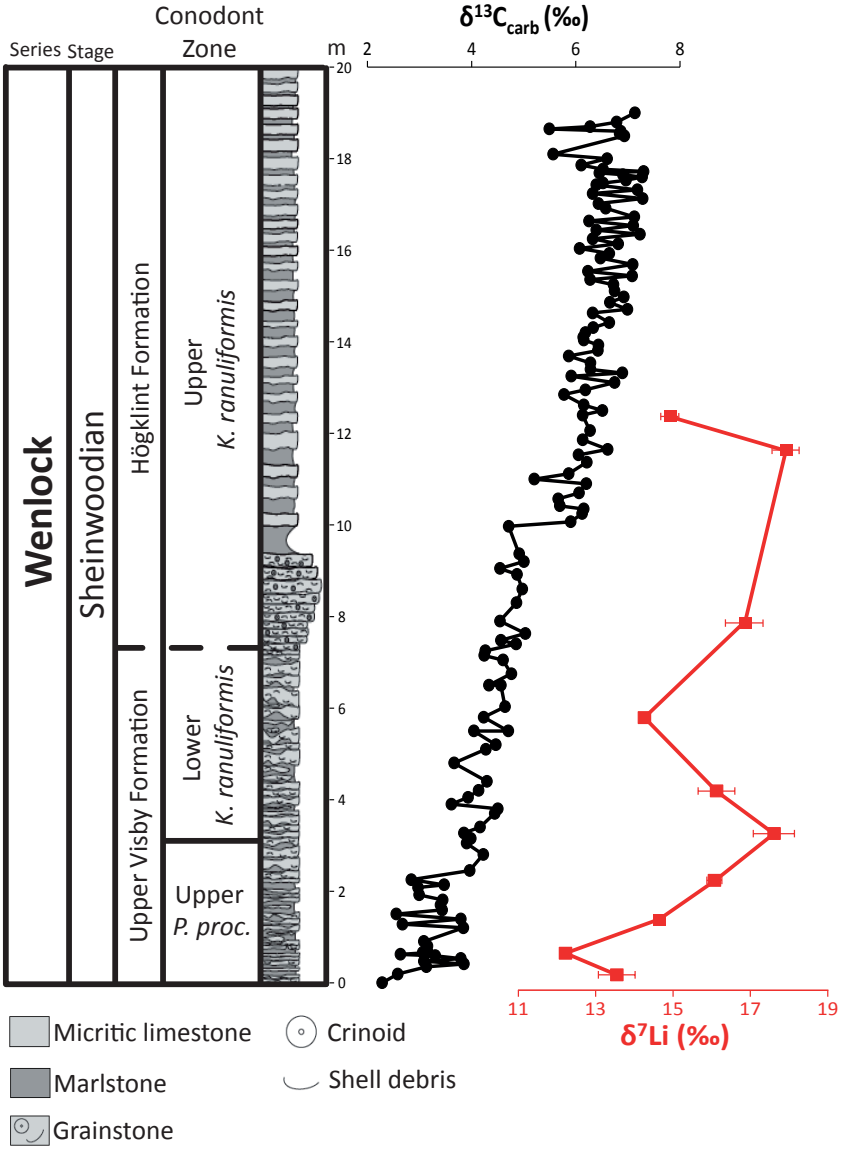

Fig. S6. Lithium (δ^7Li, red squares) and carbon ($\delta^{13}C_{carb}$, black circles) isotope ratios for carbonates from the Llandovery-Wenlock Lickershamn section. Biozone, lithology and carbon isotope data have been adapted from Maier (2010). See text for details.

2.2.3 Hunninge-1 drillcore

The Mg/Ca, Al/Ca, Mn/Ca and Sr/Ca ratios are variable throughout the Hunninge-1 drillcore (Mg/Ca = 3.7 to 185.5 mmol/mol; Al/Ca = -0.005 to 1 mmol/mol; Mn/Ca = 0.15 to 3.64 mmol/mol; Sr/Ca = 0.07 to 1.98 mmol/mol; Table S2). Many of the Al/Ca ratios remain below the ~0.8 mmol/mol threshold, except for samples at -1.5 m and 0.2 m which have an Al/Ca ratio of 1 suggesting potential influence from Li leached from clays. However, these samples have almost identical δ^7Li values to surrounding samples suggesting that the overall trend remains the same. The δ^7Li values range from 7.9 to 14.7 ‰ (Table S2; Fig. S7). From -5.8 to 1.8 m, δ^7Li rises from 10 ‰ to 14.7 ‰. After this, δ^7Li values remain relatively constant (~13.5 ‰) before decreasing to minimum values of 7.9 ‰ at 15.05 m.

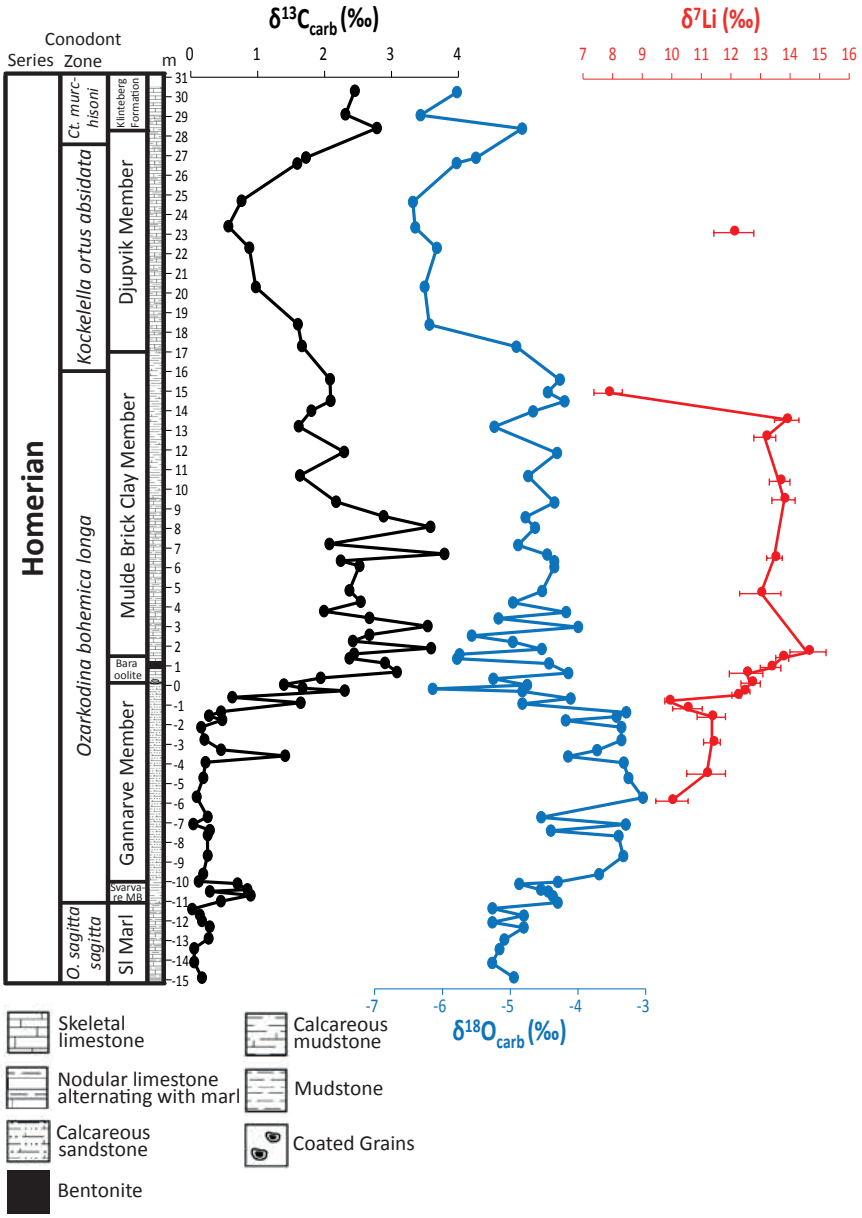

Fig. S7. Lithium (δ^7Li, red circle), oxygen ($\delta^{18}O_{carb}$, blue circles) and carbon ($\delta^{13}C_{carb}$, black circles) isotope ratios for carbonates from the Homerian Hunninge-1 core. Biozone, lithology, and carbon and oxygen isotope data have been adapted from Calner *et al*. (2006). See text for details.

2.2.4 Kosov section

The Mg/Ca, Al/Ca, Mn/Ca and Sr/Ca ratios are variable throughout the Kosov section (Mg/Ca = 10.93 to 14.6 µmol/mol; Al/Ca = 0.01 to 0.2 µmol/mol; Mn/Ca = 0.31 to 1.23 µmol/mol; Sr/Ca = 0.44 to 0.99 µmol/mol; Table 3). Al/Ca remains below the 0.8 mmol/mol threshold, suggesting little influence from Li leached from clays. The δ^7Li values range from 4.6 to 15.4 ‰ (Table S2; Fig. S3). From 4.77 to 1 m, below the base of the *Pristiograptus dubius postfrequens* Biozone, δ^7Li decreases from 9.6 to 4.6 ‰. Between 1 and 0.05 m, the δ^7Li increases from 4.6 to 15.4 ‰ before decreasing again to 5.3 ‰ by -1.15 m. The δ^7Li values remain relatively constant at ~6 ‰ before subsequently increasing to 12.8 ‰ between -4.05 and -5.28 m.

3. Age-depth models

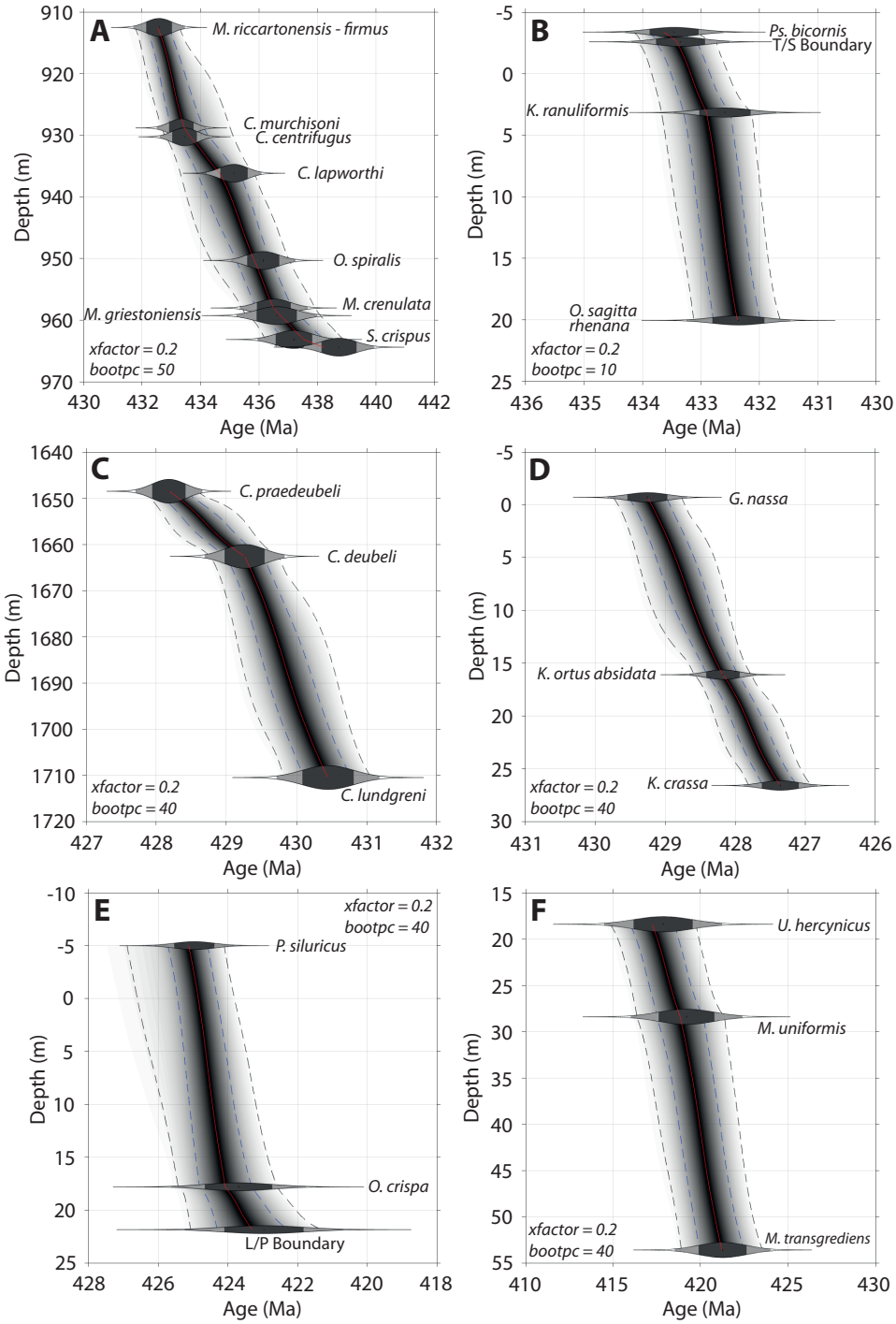

Fig. S8. *Undatable* age-depth model for the Aizpute-41 (**A**), Lusklint & Lickershamn (**B**) Bartoszyce IG-1 (**C**), Hunninge-1 (**D**), Kosov (**E**) and Klonk (**F**) sections based on graptolite biozone, conodont biozone and stage boundary ages from GTS 2012 and 2016. The red line, blue broken line and black broken line represent the median, 1σ confidence and 2σ confidence intervals, respectively.

An accurate age-model is essential for determining the timing of Os and Li isotope variation recorded in all Silurian sections studied here. We therefore used the age-depth modelling routine, *Undatable*, which uses the Bayesian calibration software, *MatCal*, taking into account both depth and analytical uncertainties (Lougheed and Obrochta, 2019). *Undatable* is built to utilize radiocarbon ^{14}C dates, assuming positive accumulation rates, but here we have applied it to Silurian sections using graptolite biozone, conodont biozone and stage boundary ages from the Geological Time Scale (GTS) 2012 and 2016 (Melchin et al., 2012; Ogg et al., 2016). Analytical uncertainty is derived from the 2σ spline error reported in GTS 2012 and 2016 while depth uncertainty varies with each section but generally falling within the range of 0.1 to 0.2 m. Due to the low number of age-depth points in the sections studied here, a relatively high *xfactor* and *bootpc* value of 0.2 and 10-50 are used to increase the variability between age-depth points and explore a higher number of routing possibilities, respectively (Lougheed and Obrochta, 2019). For the Hirnantian, only the *Metabolograptus persculptus* graptolite biozone is recorded for the Pointe Laframboise section (Melchin et al., 2013; Pogge von Strandmann et al., 2017) so *Undatable* is not used. Instead, for the Pointe Laframboise and Dob's Linn section we use a linear interpolation between ages, and associated uncertainty, reported for the upper and lower boundary of the *Me. persculptus* zone in GTS 2012 (Melchin et al., 2012). The new age-depth models are presented in Fig. S8.

4. Dynamic C-Os-Li geochemical model description

A description of the dynamic model used in this study can be found below. Additionally, a supplementary Excel file contains all the calculations used to produce Fig. 3, 5, 6, 7, S9 and S10.

4.1 Global temperature and ice sheet extent

We replace the original (Pogge von Strandmann et al., 2017) simple formula for global temperature change (relative to the present day 15°C), which used a 2.8°C climate sensitivity (the response to doubling/halving CO_2) and a 5.8°C cooling due to lower solar luminosity at 450 Ma, with a fit to the coupled GCM-ice sheet model results of Pohl *et al.* (2016) which use a 450 Ma (Late Ordovician) palaeogeography and lowered solar luminosity (black line in their Fig. 3a). Plate tectonic reconstructions indicate that the key features of a Southern Hemisphere supercontinent covering the pole and a Northern Hemisphere dominated by ocean persisted throughout the Silurian. Hence the key features of Pohl et al.'s climate-ice sheet simulations are expected to have been present throughout the Silurian – in particular, the potential for reductions in CO_2 to trigger abrupt ice sheet growth on the south pole (as well as abrupt expansion of sea-ice on the north pole).

Our initial model precludes glaciation (i.e. has no change in ice sheet area) and for that we use the temperature results of Pohl *et al.* (2016) for a largely ice-free world (CO_2 = 16 to 24 PAL), assuming a logarithmic relationship between CO_2 and radiative forcing, but extrapolating the corresponding climate sensitivity (~3.1°C) to lower CO_2 and temperature:

$$\Delta T = 4.439*\ln(CO_2) + 11.592 - 15 \quad \text{Eq. S1}$$

where 15 (°C) represents the present-day global temperature. Note that this formula implies (for present day CO_2) a 3.4°C cooling due to the combination of lower solar luminosity, ice sheet removal, and altered palaeogeography at 450 Ma.

A variant of our model includes interactive ice sheets and their effect on temperature, fitting all the results of Pohl *et al.* (2016) (see their Fig. 3a). Again, following well-established physics, we assume that a logarithmic relationship between CO_2 and radiative forcing is retained throughout, but here the corresponding climate sensitivity and temperature change depends on the state of ice sheet feedbacks. Pohl *et al.*(2016) capture this by drawing straight lines in log(CO_2)-temperature space between their results at specific CO_2 values.

For $24 > CO_2 > 16$ PAL: $\Delta T = 4.439*\ln(CO_2) + 11.592 - 15$ Eq. S2

For $16 > CO_2 > 12$ PAL: $\Delta T = 13.557*\ln(CO_2) - 13.688 - 15$ Eq. S3

For $12 > CO_2 > 8$ PAL: $\Delta T = 4.933*\ln(CO_2) + 7.743 - 15$ Eq. S4

For $8 > CO_2 > 3$ PAL: $\Delta T = 14.274*\ln(CO_2) - 11.682 - 15$ Eq. S5

This captures a large increase in climate sensitivity to ~9.4°C as ice sheets abruptly expand in the range $16 > CO_2 > 12$ PAL, reversion to a typical climate sensitivity ~3.4°C as their area stabilises at $12 > CO_2 > 8$ PAL, then increased climate sensitivity of ~9.9°C as sea-ice abruptly expands in the range $8 > CO_2 > 3$ PAL. Note that the ice cover and temperature changes are likely even more non-linear 'tipping points' with respect to CO_2 change than captured here, it is just that Pohl *et al.* have a limited set of simulations at 3, 8, 10, 12, 16 and 24 PAL CO_2.

We also fit Pohl *et al.*'s (2016) results for ice sheet (IS) extent (Mkm^2, red line in their Fig. 3a):

For $CO_2 < 24$ and $CO_2 > 16$ PAL, $IS = -4.933*\ln(CO_2) + 15.676$ Eq. S6

For $CO_2 < 16$ and $CO_2 > 12$ PAL, $IS = -121.662*\ln(CO_2) + 339.319$ Eq. S7

For $CO_2 < 12$ and $CO_2 > 8$ PAL, $IS = -4.933* \ln(CO_2) + 49.257$ Eq. S8

For $CO_2 < 8$ and $CO_2 > 3$ PAL, $IS = -11.215*\ln(CO_2) + 62.321$ Eq. S9

In the initial model where glaciation is precluded, IS extent is fixed at the value corresponding to initial CO_2. To convert IS extent to volume (with corresponding effects on sea level and $\delta^{18}O$) we explore different average ice sheet thicknesses. Pohl *et al.*(2016) constrain the Hirnantian glaciation to an average thickness of ~3 km. Considering that we expect Silurian ice sheets to have been smaller and more ephemeral than those of the Late Ordovician, we use a default ice thickness of 1 km but run sensitivity tests using a thickness of 2 and 3 km.

4.2 Carbon cycle

Atmospheric CO_2 is normalised to the present atmospheric level (PAL):

$$CO_2 = (A/A_0)^2 \quad \text{Eq. S10}$$

where A represents the ocean-atmosphere reservoir, $A_0 = 3.2 \times 10^{18}$ mol C.

The overall carbon balance is:

$$dA/dt = F_d - F_w - F_{org} \quad \text{Eq. S11}$$

where F_d is the degassing input flux of CO_2, F_w is the silicate weathering (and subsequent carbonate burial) flux of CO_2 consumption, and F_{org} represents a potential orbital-driven accumulation (or if negative a decay) of a quasi-stable sedimentary organic carbon reservoir, where $F_{org} = 0$ in the absence of orbital forcing. This approach assumes carbonate weathering is balanced by a corresponding flux of carbonate burial (following GEOCARB III) and that oxidative weathering is balanced by a corresponding organic carbon burial flux.

Degassing (F_d) is subject to a normalised forcing parameter, D, linked to seafloor spreading rates:

$$F_d = k_1*D \quad \text{Eq. S12}$$

where $k_1 = 8 \times 10^{12}$ molC/yr (Kump and Arthur, 1999).

The treatment of the silicate weathering flux, based on COPSE (Lenton et al., 2018) and GEOCARBSULF (Berner, 2006), is more sophisticated than Pogge von Strandmann *et al.* (2017). Given the existence of partial plant cover in the Silurian, it recognises separate abiotic and biotic components of the weathering response. Silicate weathering depends on atmospheric CO_2, temperature effects on weathering kinetics, f(T), and runoff, g(T), the normalised forcing of uplift (U), and vegetation (V) and its effect on weathering (W):

$$F_w = k_1*U*(k_2*CO_2^{0.5}+(1–k_2)*V*W*f(CO_2))*f(T)*g(T) \quad \text{Eq. S13}$$

where k_2^{-1} represents the amplification of weathering rates by today's vegetation, and we find $k_2 = 0.1$ (10-fold amplification) provides a good initialisation of CO_2. The first term in brackets in Eq. S13 represents the abiotic response of weathering to $CO_2^{0.5} = A/A_0$. The second term represents the biotic response of weathering where photosynthesis has a Michaelis-Menten relationship to CO_2:

$$f(CO_2) = 2*CO_2/(1+CO_2) \quad \text{Eq. S14}$$

Silicate weathering kinetics depend directly on temperature:

$$f(T) = e^{0.09*\Delta T} \quad \text{Eq. S15}$$

where the factor 0.09 corresponds to an activation energy of 62 kJ mol^{-1}. Weathering also depends on runoff, which depends on temperature:

$$g(T) = (1 + 0.038*\Delta T)^{0.65} \quad \text{Eq. S16}$$

Silicate weathering provides negative feedback on changes in atmospheric CO_2 and temperature that may be driven by changes in tectonic (D, U), biological (V, W), or orbital forcing parameters.

4.3 Orbital forcing of carbon cycle imbalances

We explore the hypothesis of orbital-driven changes in the organic carbon cycle, adapting the threshold response model of Laurin *et al.* (2015). This assumes that when the precession index or axial obliquity fall below a threshold value (th1), a quasi-stable organic carbon reservoir, C_{org}, builds up. Between th1 and another threshold (th2) the reservoir remains stable, and above th2 the reactive reservoir decays, returning carbon back to the ocean-atmosphere. C_{org} is initialised at zero, accumulated by R_{build} and drained by R_{decay} (to a minimum of zero).

$$\text{For op} < \text{th1}, F_{org} = R_{build}$$
$$\text{For th1} < \text{op} < \text{th2}, F_{org} = 0$$
$$\text{For op} > \text{th2}, \text{if } C_{org} \geq R_{decay}*\Delta t \text{ then } F_{org} = –R_{decay}, \text{ else } F_{org} = –C_{org}/\Delta t \quad \text{Eq. S17}$$

where op is the precession index or axial obliquity. The precession index and obliquity series were obtained with the numerical solutions from La04 for 9.6 to 10.6 Ma and 9.4 to 11.6 Ma, respectively (Fig. 4). We apply this forcing to the marine organic carbon reservoir, assuming that insolation directly forces the burial and decay of organic carbon on continental margins and epeiric seaways via changes in annual precipitation, runoff and nutrient flux (Kocken et al., 2019; Laurin et al., 2015). Under weaker forcing, burial of isotopically light (C^{12}) and therefore atmospheric CO_2 sequestration occurs, becoming reversed under stronger forcing.

Although not explored here, reduced insolation would also have led to oceanic cooling and the storage of biogenic methane as isotopically light ($\delta^{13}C = < -70$) methane hydrates, influencing planetary climate and marine $\delta^{13}C$ records (Kocken et al., 2019). An alternative to the marine organic carbon reservoir is the storage of terrestrial organic carbon due to higher phosphorous weathering and primary productivity during the development of early land plants in the Late Ordovician and Silurian (Lenton et al., 2016). However, here we keep the terrestrial organic carbon flux constant for simplicity.

4.4 Lithium cycle model

A modified version of the dynamic, non-steady state, box model from Pogge von Strandmann *et al.* (2017) is used to explore the response of lithium and its isotopes. The dynamic mass balance equation for Li is as follows:

$$dN_{Li}/dt = F_{riv} + F_{hyd} - F_{sink} \quad \text{Eq. S18}$$

where N_{Li} is the seawater Li reservoir, F_x (riv = river, hyd = hydrothermal, sink = combined uptake in marine sediments and alteration of oceanic crust) represents the input and output fluxes. The isotopic mass balance equation for Li is:

$$N_{Li}*dR_{sw}/dt = F_{riv}(R_{riv} - R_{sw}) + F_{hyd}(R_{hyd} - R_{sw}) - F_{sink}(R_{sink} - R_{sw}) \quad \text{Eq. S19}$$

where R_x is the isotope ratio of the various fluxes, $R_{sink} - R_{sw} = \Delta_{sink}$, and F_{sink} is the sink of Li from seawater relative to a constant partition coefficient, k_{Li}:

$$F_{sink} = k_{Li}*N_{Li} \quad \text{Eq. S20}$$

where k_{Li} is the inverse of the residence time of Li in the ocean and initially we use $k_{Li} = 7.12 \times 10^{-7}$ yr^{-1}. The R_{sw} (Eq. S18) is converted to that of carbonate (R_{carb}) by subtracting a 4 ‰ fractionation factor (Marriott et al., 2004). The R_{riv} is assumed to depend on glaciation, increasing with IS area (Mkm^2):

$$R_{riv} = 0+10*(IS/35) \quad \text{Eq. S21}$$

The riverine flux of Li is assumed to be proportional to the silicate weathering flux (Eq. S12, which balances degassing):

$$F_{riv} = k_{riv}*F_w/k_1 \quad \text{Eq. S22}$$

where $k_{riv} = 1.29 \times 10^{10}$ molLi/yr.

The hydrothermal flux of Li scales with seafloor spreading rates and therefore degassing:

$$F_{hyd} = k_{hyd}*D \quad \text{Eq. S23}$$

where $k_{hyd} = 6 \times 10^9$ molLi/yr.

4.5 Osmium cycle model

The behaviour of Os and its isotopes through time was modelled using a modified version of the dynamic, non-steady state, box model of Pogge von Strandmann *et al.* (2013) and Lechler *et al.* (2015). Unlike previous models, the riverine flux of Os is partitioned into fluxes from a range of lithologies relevant to Os. The dynamic mass balance equation for Os is as follows:

$$dN_{Os}/dt = F_{gra} + F_{bas} + F_{sed} + F_{cos} + F_{hth} - F_{out} \quad \text{Eq. S24}$$

where N_{Os} is the seawater Os reservoir, F_x (gra = granite, bas = basalt, sed = sedimentary rock, cos = cosmogenic, hth = high-temperature hydrothermal, out = Os sinks) represents the input and output fluxes. The isotopic mass balance equation for Os is:

$$N_{Os}*dR_{sw}/dt = F_{gra}(R_{gra} - R_{sw}) + F_{bas}(R_{bas} - R_{sw}) + F_{sed}(R_{sed} - R_{sw}) + F_{cos}(R_{cos} - R_{sw}) + F_{hth}(R_{hth} - R_{sw}) - F_{out}(R_{out} - R_{sw}) \quad \text{Eq. S25}$$

where R_x is the isotope ratio of the various fluxes and F_{out} is the sink of Os from seawater relative to a constant partition coefficient, k_{Os} (3.37×10^{-5}) corresponding to a ~30 kyr residence time:

$$F_{out} = k_{Os}*N_{Os} \quad \text{Eq. S26}$$

The riverine Os flux from the weathering of silicates, is split into granite and basalt components, to capture the impact of altered lithology on initial isotopic composition of seawater:

$$F_{gra} = k_{gra}*(1 - f_{bas}*A_{bas})*F_{sil}/((1- f_{bas})*k_1) \quad \text{Eq. S27}$$

$$F_{bas} = k_{bas}*f_{bas}*A_{bas}*F_{sil}/(f_{bas}*k_1) \quad \text{Eq. S28}$$

Where $f_{bas} = 0.25$ is the fractional contribution of volcanic rocks to the silicate weathering flux today, A_{bas} is the relative area of volcanic rocks compared to today, $k_{gra} = 551$ mol Os/yr and $k_{bas} = 654$ mol Os/yr (Li and Elderfield, 2013). $A_{bas} = 2$ is used to lower initial

$^{187}Os/^{188}Os$ on the grounds that there were extensive volcanic arcs in the Late Ordovician-Silurian.

The riverine Os flux from sedimentary weathering includes the contribution of Os-rich lithologies (Georg et al., 2013). It is assumed to scale with uplift and associated erosion, and a lithology exposure factor (A_{sed}):

$$F_{sed} = k_{sed}*A_{sed}*U \quad \text{Eq. S29}$$

where k_{sed} = 1119 mol Os/yr. A_{sed} = 0.75 is used to lower initial $^{187}Os/^{188}Os$ on the grounds that following the 'great discontinuity' and without vegetation beforehand, there was less sedimentary rock exposed in the Silurian than today, including less shale exposure than today.

The hydrothermal flux of Os scales with seafloor spreading rates and therefore degassing:

$$F_{hth} = k_{hth}*D \quad \text{Eq. S30}$$

where k_{hth} = 56 mol Os/yr.

The extra-terrestrial flux of Os is assumed to be constant throughout at F_{cos} = 115 molOs/yr.

In the sensitivity analysis, we explore the hypothesis that glaciation and associated erosion increased sedimentary weathering in proportion to ice sheet area, up to a factor of ~2:

$$F_{sed} = k_{sed}*A_{sed}*(U + (IS/35)) \quad \text{Eq. S31}$$

which replaces Eq. S29

4.6 Carbon isotopes, oxygen isotopes and sea-level

We include a simple isotopic mass balance of carbon:

$$A*d\delta_C/dt = (F_d + k_c)*(-5 - \delta_C) - (k_b + F_{org})* \Delta_{org} \quad \text{Eq. S32}$$

where $k_c = 17 \times 10^{12}$ molC yr^{-1} is the input of carbon from carbonate and oxidative weathering (assumed fixed and with average composition -5‰) and $k_b = 7 \times 10^{12}$ molC yr^{-1} is the burial of organic carbon that balances oxidative weathering (assumed fixed). Δ_{org} = 25‰ is the fractionation with incorporation in organic matter.

The oxygen isotopic composition of conodont apatite ($\delta^{18}O_{phos}$) depends on the $\delta^{18}O$ of seawater ($\delta^{18}O_{sw}$) and temperature and can be calculated following (Joachimski et al., 2009; Trotter et al., 2008; Trotter et al., 2016):

$$\delta^{18}O_{phos} = (SST - 113.3)/-4.39 + \delta^{18}O_{sw} \quad \text{Eq. S33}$$

where SST is tropical sea surface temperature, converted from global surface air temperature using a general offset of ~8°C for the Hirnantian (Pohl et al., 2016), and $\delta^{18}O_{sw}$ is -1 ‰ for the Palaeozoic (Joachimski et al., 2009; Trotter et al., 2008; Trotter et al., 2016). When ice sheet extent is introduced, $\delta^{18}O_{sw}$ becomes dependent on global sea-level at a rate of 0.01 ‰/m (Rohling, 2013) following Horton *et al.* (2007):

$$IVSLE = WE/SA_{ocean} \quad \text{Eq. S34}$$

where the ice volume water equivalent, WE, is converted from IV using ice density of 0.917 Gt/km^3 and SA_{ocean} refers to the Silurian ocean surface area (361.8×10^6 km^2). Final sea-level estimations are reported as isostatically adjusted sea-level equivalent (IASLE):

$$IASLE = 1/k*WE/SA_{ocean} \quad \text{Eq. S35}$$

where k is the ratio of seawater density to oceanic lithosphere density (0.284) (Horton et al., 2007).

4.7 Integration

The model is solved numerically using Euler's method with a 5000 yr timestep.

4.8 Model assumptions and caveats

The dynamic C-Os-Li geochemical model developed here should be viewed as a minimal model designed to capture key feedbacks and controls on the proxy data we consider, but deliberately leaving out large parts of the Earth's biogeochemical cycles in the interests of clarity and simplicity. It captures key aspects of the global inorganic carbon cycle using fluxes, baseline values and equations from the GEOCARBSULF (Berner, 2006) and COPSE (Lenton et al., 2018) biogeochemical models for carbon degassing and biotic and abiotic silicate weathering. The model does not distinguish seafloor weathering, but that provides comparable negative feedback on CO_2 and temperature change as terrestrial silicate weathering. Carbonate weathering and burial are assumed to remain in balance (as in the longer-term models), but orbitally driven carbon cycle fluctuations and glaciations in the Late Ordovician-Silurian would likely have driven them out of balance on ~10 kyr timescales. Whilst this could alter the ~10 kyr timescale CO_2 variations predicted, e.g., Fig. 5 of the main paper, it would not be expected to alter the >100 kyr timescale variations in CO_2, climate, and isotope proxies.

A key difference from GEOCARBSULF or COPSE is the treatment of the organic carbon cycle. As our focus is on timescales of up to ~2 Myr it is reasonable to consider oxidative weathering and organic carbon burial in new sedimentary rocks to be in approximate balance (Lenton et al., 2018). However, we include the possibility of a transient organic carbon reservoir that can build up and be drained on shorter, orbital timescales. This orbitally-sensitive reservoir introduced by others (Laurin et al., 2015), and the magnitude of input and output fluxes to it, should be viewed as a working hypothesis. The corresponding fluxes are calibrated to generate the observed timescale and magnitude of carbon isotope variability and need to be surprisingly large. Future work with more detailed models needs to take a more process-based approach to assessing whether and how such significant, short-term organic carbon cycle imbalances can be generated by orbital forcing coupled with climate, cryosphere, and sea-level changes.

The other key distinction from existing carbon cycle models is the use of relevant general circulation model (GCM) results (Pohl *et al.* (2016)) to calibrate global temperature and ice sheet functions specific to the Late Ordovician-Silurian period. Here an important assumption is that the strongly non-linear climate feedbacks discovered for the 450 Ma paleogeography of the GCM, hold as paleogeography changes somewhat during the Silurian. Further GCM runs could interrogate this assumption, noting that we already argue from sea-level and oxygen isotope proxies that ice sheet growth was less thick in the Silurian than the Hirnantian. The functional fits to GCM results that we use enfold the effects of large southern hemisphere ice sheets and changes in sea-ice on global temperature. However, the feedback effects of ice sheet and sea-level changes on the carbon cycle are not considered. For example, retreat of ice sheets would expose freshly ground glaciogenic sediments to weathering, and a drop in sea-level would expose marine sediments to weathering.

Although the threshold response model of Laurin *et al.* (2015) is linked to organic carbon cycling, obliquity and precession variations in the seasonal contrast and latitudinal distribution of insolation would also be expected to directly drive changes in climate and ice sheet extent independently of changes in the atmospheric CO_2. To capture this needs a more detailed climate model. Furthermore, obliquity and precession forcing are treated separately, whereas their effects are combined. Unfortunately, the lack of numerical solutions for the Earth's orbital parameters beyond 250 Ma and their lack of precision beyond 40-50 Ma (Laskar et al., 2011; Laskar et al., 2004) precludes direct comparison of obliquity, eccentricity and precession parameters with Paleozoic climate records.

Our simple model omits nitrogen, phosphorus and sulphur cycling, ocean redox, or atmospheric O_2 variation (driven by simulated transient imbalances in the organic carbon cycle). Including these variables in future work would provide a more complete view of

Hirnantian and Silurian climate events, for example, seeking to capture changes in marine productivity, ocean redox state and the formation of black shales.

Table S3. Definitions of model parameters.

Symbol	Parameter	Value	Reference
Forcing factors			
D	Volcanic and metamorphic degassing (normalised)	1.5	(Lenton et al., 2018)
U	Tectonic uplift (normalised)	0.94	(Lenton et al., 2018)
V	Plant evolution and land colonisation (normalised)	0.15	(Lenton et al., 2018)
W	Plant enhancement of weathering (normalised)	0.75	(Lenton et al., 2018)
Carbon cycle			
th1	Precession or obliquity threshold 1	0.024 or 23.6	(Laurin et al., 2015)
th2	Precession or obliquity threshold 2	0.0259 or 23.63	(Laurin et al., 2015)
R_{build}	Build up rate for bulk organic carbon reservoir	1.13 or 1.19 x 10^{13} molC yr^{-1}	This study
R_{decay}	Decay rate for bulk organic carbon reservoir	7.59 or 3.17 x 10^{13} molC yr^{-1}	This study
A_0	Present day size of atmosphere-ocean CO_2 reservoir	3.2 x 10^{18} mol	(Lenton et al., 2018)
k_1	Silicate weathering flux	8 x 10^{12} molC yr^{-1}	(Pogge von Strandmann et al., 2017)
k_2	Abiotic relative rate of weathering	0.1	(Lenton et al., 2018)
Osmium cycle			
k_{os}	Partition coefficient of oceanic Os sink	3.37 x 10^{-5} yr^{-1}	This study
f_{bas}	Contribution of volcanic rocks to silicate weathering	0.25	(Lenton et al., 2018)
A_{bas}	Relative exposure of volcanic silicate rocks	2	This study
A_{sed}	Relative exposure of sediments including shales	0.75	This study
k_{gra}	Granite weathering flux	551 molOs yr^{-1}	(Li and Elderfield, 2013)
k_{bas}	Basalt weathering flux	654 molOs yr^{-1}	(Li and Elderfield, 2013)
k_{sed}	Bulk sedimentary weathering flux	1119 molOs yr^{-1}	(Li and Elderfield, 2013)
k_{hth}	Hydrothermal flux	56 molOs yr^{-1}	(Li and Elderfield, 2013)
F_{cos}	Cosmogenic flux	115 molOs yr^{-1}	(Li and Elderfield, 2013)
R_{gra}	Isotope ratio of granite	1.05	(Li and Elderfield, 2013)
R_{bas}	Isotope ratio of basalt	0.126	(Li and Elderfield, 2013)
R_{sed}	Isotope ratio of bulk sediments	1.78	(Li and Elderfield, 2013)
R_{hth}	Isotope ratio of hydrothermal source	0.126	(Li and Elderfield, 2013)
R_{cos}	Isotope ratio of cosmogenic source	0.126	(Li and Elderfield, 2013)
Lithium cycle			
k_{li}	Partition coefficient of oceanic Li sink	7.12 x 10^{-7} yr^{-1}	(Pogge von Strandmann et al., 2017)
k_{riv}	Riverine flux	1.29 x 10^{10} molLi yr^{-1}	(Pogge von Strandmann et al., 2017)
k_{hyd}	Hydrothermal flux	6 x 10^{9} molLi yr^{-1}	(Pogge von Strandmann et al., 2017)
R_{riv}	Isotope ratio of riverine source	0 to 20 ‰	(Pogge von Strandmann et al., 2017)
R_{hyd}	Isotope ratio of hydrothermal source	7 ‰	(Pogge von Strandmann et al., 2017)
Δ_{sink}	Fractionation of sink from seawater	14.86 ‰	(Pogge von Strandmann et al., 2017)

4.9 Sensitivity tests

4.9.1 Degassing

The normalised forcing factor for volcanic and metamorphic degassing, D, varies between 1 and 1.8 during the Phanerozoic (541 Ma to the present) in both the GEOCARBSULF (Royer et al., 2014) and COPSE (Lenton et al., 2018) models (see Fig. 3a in Lenton et al. (2018)). In the current model for Late Ordovician and Silurian climate events (Fig. 3A-C), degassing is reduced over 1 Myr from early Silurian estimates (1.5) to an extreme value (0.75) not feasible for the Phanerozoic (Fig. 3A). If we reduce D over 1 Myr from 1.5 to 1.3 (Fig. S9A), more in keeping with values estimated for the late Silurian to Early Devonian (see Fig. 3a in Lenton et al. (2018)), we observe a more muted response, decreasing atmospheric CO_2 by ~2.5 PAL and temperature by ~0.8 °C (Fig. S9B), driving an increase in $\delta^{18}O_{phos}$ of ~0.2 ‰ (Fig. S9C). The reduced riverine and hydrothermal fluxes coupled to a reduction in the oceanic Li reservoir drives a ~0.7 ‰ positive δ^7Li excursion over ~3 Myr (Fig. S9C). Ocean Os content drops more rapidly, and because the unradiogenic hydrothermal and basalt weathering input is reduced, the $^{187}Os/^{188}Os$ of seawater increases by ~0.14 (Fig. S9C).

Revisiting the original model in Fig. 3A, but with a more rapid halving of D over 0.5 Myr (dashed line in Fig. S9D) causes the same variation in atmospheric CO_2, temperature, $^{187}Os/^{188}Os$, δ^7Li and $\delta^{18}O_{phos}$ as the original model (Fig. 3B-C) but over ~2 Myr (dashed lines in Fig. S9E-F). A doubling of the duration over which D halves to 2 Myr (solid line in Fig. S9D) prolongs the variation, which now occurs over ~4 Myr (solid lines in Fig. S9E-F). These sensitivity tests suggest that varying D or the duration over which D declines can influence the magnitude and duration of changes in atmospheric CO_2, temperature, $^{187}Os/^{188}Os$, δ^7Li and $\delta^{18}O_{phos}$ (Fig. S9). However, the change in Os, Li and O remains a permanent shift to higher values, unlike the transient variation observed in Hirnantian and Silurian records (Fig. 1 and Fig. 2).

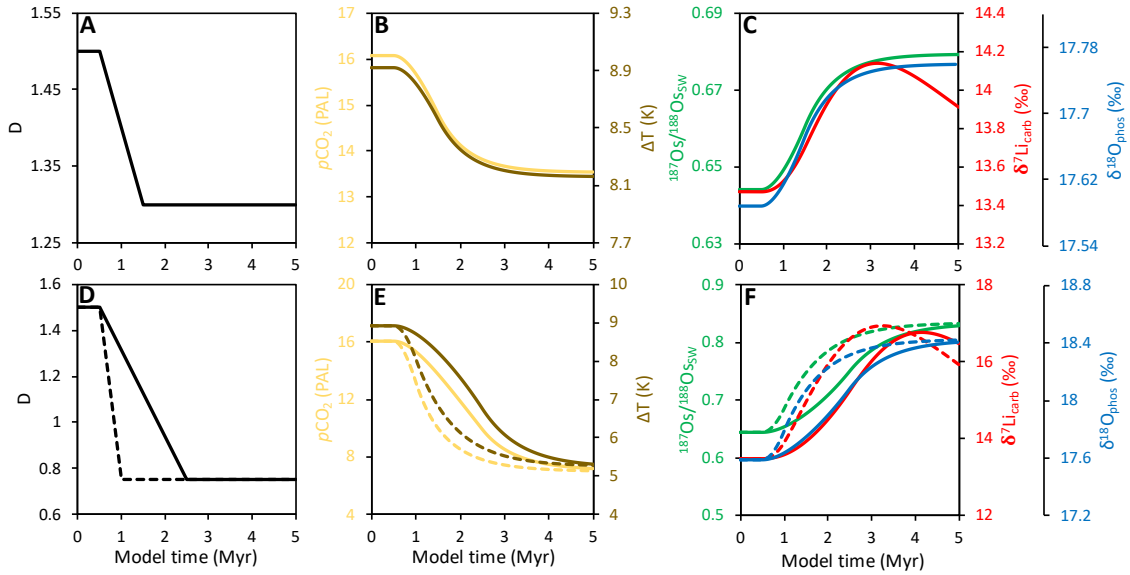

Fig. S9. The effect of degassing on the O, Os and Li isotope systems using a dynamic carbon-osmium-lithium-model. See section 4.9.1 for details.

4.9.2 Vegetation

The normalised forcing factor for plant evolution and land colonisation, V, ranges from 0-0.15 in the Ordovician to 1 by the Permian in both the GEOCARBSULF (Royer et al., 2014) and COPSE (Lenton et al., 2018) models (see Fig. 3c in Lenton et al. (2018)). In the current model for Late Ordovician and Silurian climate events (Fig. 3D-F), vegetation cover is increased from Silurian values (0.15) to estimates for the Early Devonian (0.3) (Fig. 3D). If we increase V over 1 Myr from 0.15 to 1 (Fig. S10A), estimated for the Late Devonian (see Fig. 3c in Lenton et al. (2018)), we observe a much larger response. Atmospheric CO_2 and

temperature respectively decrease by ~12 PAL and ~7 °C (Fig. S10B), driving an increase in $\delta^{18}O_{phos}$ of 0.15 ‰ (Fig. S10C). The increase in silicate weathering brought on by land plant proliferation drives a transient negative ~1.7 ‰ excursion in $\delta^{7}Li$ (Fig. S10C) because the unfractionated riverine source increases. The weathering of more radiogenic granitic and sedimentary rocks drives a similar transient decrease in the $^{187}Os/^{188}Os$ of ~0.08 (Fig. S10C).

Revisiting the original model in Fig. 3D, but with a more rapid doubling of V over 0.5 Myr (dashed line in Fig. S10D) causes a similar decline in atmospheric CO_2 and temperature, as the original model (Fig. 3B-C) but over ~2 Myr (dashed lines in Fig. S10E). The $^{187}Os/^{188}Os$ and $\delta^{7}Li$ of seawater decreases by ~0.04 and 0.55 ‰ to lower values than the original model and over a shorter duration of ~1 Myr (dashed lines in Fig. S10F). A doubling of the duration over which V increases to 2 Myr (solid line in Fig. S10D) produces a more muted response in $^{187}Os/^{188}Os$ and $\delta^{7}Li$ over ~4 Myr (solid lines in Fig. S10F).

The plant enhancement of weathering, W, is estimated to be 0.75 during the Silurian in the COPSE model, increasing to 1 by the end of the Devonian (see Fig. 3d in Lenton et al. (2018)). If we run the original vegetation scenario (Fig. 3D) with a W of 1 (Fig. S10G-I) it causes a larger silicate weathering response leading to an atmospheric CO_2 and temperature drop of ~7 PAL and ~2.5 °C, respectively (Fig. S10H). The $^{187}Os/^{188}Os$ and $\delta^{7}Li$ of seawater decreases by ~0.02 and 0.6 ‰ (Fig. S10I). These sensitivity tests suggest that varying V or the duration over which V increases can influence the magnitude and duration of changes in atmospheric CO_2, temperature, $^{187}Os/^{188}Os$, $\delta^{7}Li$ and $\delta^{18}O_{phos}$ (Fig. S10). However, the change in O remains a permanent shift to higher values, unlike the transient variation observed in Hirnantian and Silurian records (Fig. 1), and Os and Li continues to display a negative transient excursion, unlike the positive one observed in Hirnantian and Silurian records (Fig. 2).

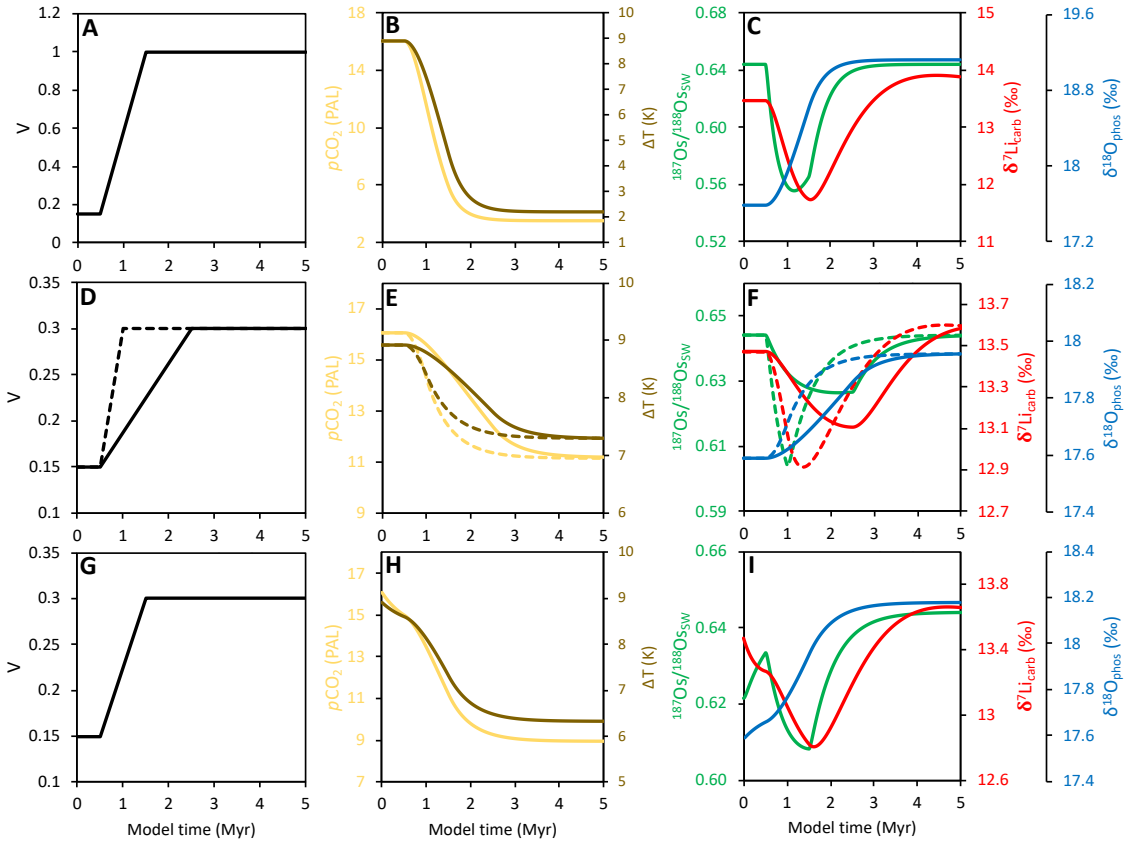

Fig. S10. The effect of vegetation on the O, Os and Li isotope systems using a dynamic carbon-osmium-lithium-model. See section 4.9.2 for details.

Supplementary references

Berner, R.A., 2006. GEOCARBSULF: A combined model for Phanerozoic atmospheric O2 and CO2. Geochimica et Cosmochimica Acta 70, 5653-5664.

Buggisch, W., Mann, U., 2004. Carbon isotope stratigraphy of Lochkovian to Eifelian limestones from the Devonian of central and southern Europe. International Journal of Earth Sciences 93, 521-541.

Calner, M., Jeppsson, L., Munnecke, A., 2004. The Silurian of Gotland—Part I: Review of the stratigraphic framework, event stratigraphy, and stable carbon and oxygen isotope development. Erlanger geologische Abhandlungen, Sonderband 5, 113-131.

Calner, M., Kozłowska, A., Masiak, M., Schmitz, B., 2006. A shoreline to deep basin correlation chart for the middle Silurian coupled extinction-stable isotopic event. GFF 128, 79-84.

Cramer, B.D., Loydell, D.K., Samtleben, C., Munnecke, A., Kaljo, D., Mannik, P., Martma, T., Jeppsson, L., Kleffner, M.A., Barrick, J.E., Johnson, C.A., Emsbo, P., Joachimski, M.M., Bickert, T., Saltzman, M.R., 2010. Testing the limits of Paleozoic chronostratigraphic correlation via high-resolution (<500 k.y.) integrated conodont, graptolite, and carbon isotope (13Ccarb) biochemostratigraphy across the Llandovery-Wenlock (Silurian) boundary: Is a unified Phanerozoic time scale achievable? Geological Society of America Bulletin 122, 1700-1716.

Crick, R., Ellwood, B., Hladil, J., El Hassani, A., Hrouda, F., Chlupac, I., 2001. Magnetostratigraphy susceptibility of the Přídolian–Lochkovian (Silurian–Devonian) GSSP (Klonk, Czech Republic) and a coeval sequence in Anti-Atlas Morocco. Palaeogeography, Palaeoclimatology, Palaeoecology 167, 73-100.

Fryda, J., Manda, S., 2013. A long-lasting steady period of isotopically heavy carbon in the late Silurian ocean: evolution of the δ13C record and its significance for an integrated δ13C, graptolite and conodont stratigraphy. Bulletin of Geosciences 88, 463-482.

Georg, R.B., West, A.J., Vance, D., Newman, K., Halliday, A.N., 2013. Is the marine osmium isotope record a probe for CO2 release from sedimentary rocks? Earth and Planetary Science Letters 367, 28-38.

Horton, D.E., Poulsen, C.J., Pollard, D., 2007. Orbital and CO2 forcing of late Paleozoic continental ice sheets. Geophysical Research Letters 34.

Joachimski, M.M., Breisig, S., Buggisch, W., Talent, J.A., Mawson, R., Gereke, M., Morrow, J.R., Day, J., Weddige, K., 2009. Devonian climate and reef evolution: Insights from oxygen isotopes in apatite. Earth and Planetary Science Letters 284, 599-609.

Kocken, I.J., Cramwinckel, M.J., Zeebe, R.E., Middelburg, J.J., Sluijs, A., 2019. The 405 kyr and 2.4 Myr eccentricity components in Cenozoic carbon isotope records. Clim. Past 15, 91-104.

Kump, L.R., Arthur, M.A., 1999. Interpreting carbon-isotope excursions: carbonates and organic matter. Chemical Geology 161, 181-198.

Laskar, J., Fienga, A., Gastineau, M., Manche, H., 2011. La2010: a new orbital solution for the long-term motion of the Earth⋆. A&A 532, A89.

Laskar, J., Robutel, P., Joutel, F., Gastineau, M., Correia, A.C.M., Levrard, B., 2004. A long-term numerical solution for the insolation quantities of the Earth. A&A 428, 261-285.

Laurin, J., Meyers, S.R., Uličný, D., Jarvis, I., Sageman, B.B., 2015. Axial obliquity control on the greenhouse carbon budget through middle- to high-latitude reservoirs. Paleoceanography 30, 133-149.

Lechler, M., Pogge von Strandmann, P.A.E., Jenkyns, H.C., Prosser, G., Parente, M., 2015. Lithium-isotope evidence for enhanced silicate weathering during OAE 1a (Early Aptian Selli event). Earth and Planetary Science Letters 432, 210-222.

Lenton, T.M., Dahl, T.W., Daines, S.J., Mills, B.J.W., Ozaki, K., Saltzman, M.R., Porada, P., 2016. Earliest land plants created modern levels of atmospheric oxygen. Proceedings of the National Academy of Sciences 113, 9704.
Lenton, T.M., Daines, S.J., Mills, B.J.W., 2018. COPSE reloaded: An improved model of biogeochemical cycling over Phanerozoic time. Earth-Science Reviews 178, 1-28.
Li, G., Elderfield, H., 2013. Evolution of carbon cycle over the past 100 million years. Geochimica et Cosmochimica Acta 103, 11-25.
Lougheed, B.C., Obrochta, S.P., 2019. A Rapid, Deterministic Age-Depth Modeling Routine for Geological Sequences With Inherent Depth Uncertainty. Paleoceanography and Paleoclimatology 34, 122-133.
Loydell, D., Männik, P., Nestor, V., 2003. Integrated biostratigraphy of the lower Silurian of the Aizpute-41 core, Latvia. Geological Magazine 140, 205-229.
Maier, G., 2010. Development of d13Ccarb and d13Corg isotope values from the Lower Silurian of Gotland (Sweden). GeoZentrum Nordbayern & Friedrich–Alexander University Erlangen–Nürnberg, p. 62.
Marriott, C.S., Henderson, G.M., Crompton, R., Staubwasser, M., Shaw, S., 2004. Effect of mineralogy, salinity, and temperature on Li/Ca and Li isotope composition of calcium carbonate. Chemical Geology 212, 5-15.
Melchin, M.J., Mitchell, C.E., Holmden, C., Štorch, P., 2013. Environmental changes in the Late Ordovician–early Silurian: Review and new insights from black shales and nitrogen isotopes. GSA Bulletin 125, 1635-1670.
Melchin, M.J., Sadler, P.M., Cramer, B.D., Cooper, R.A., Gradstein, F.M., Hammer, O., 2012. Chapter 21 - The Silurian Period, in: Gradstein, F.M., Ogg, J.G., Schmitz, M.D., Ogg, G.M. (Eds.), The Geologic Time Scale. Elsevier, Boston, pp. 525-558.
Munnecke, A., Samtleben, C., Bickert, T., 2003. The Ireviken Event in the lower Silurian of Gotland, Sweden – relation to similar Palaeozoic and Proterozoic events. Palaeogeography, Palaeoclimatology, Palaeoecology 195, 99-124.
Ogg, J.G., Ogg, G., Gradstein, F.M., 2016. A concise geologic time scale: 2016. Elsevier.
Pogge von Strandmann, P.A., Desrochers, A., Murphy, M., Finlay, A., Selby, D., Lenton, T., 2017. Global climate stabilisation by chemical weathering during the Hirnantian glaciation. Geochemical Perspectives Letters 3, 230-237.
Pogge von Strandmann, P.A.E., Jenkyns, H.C., Woodfine, R.G., 2013. Lithium isotope evidence for enhanced weathering during Oceanic Anoxic Event 2. Nature Geoscience 6, 668.
Pohl, A., Donnadieu, Y., Le Hir, G., Ladant, J.-B., Dumas, C., Alvarez-Solas, J., Vandenbroucke, T.R.A., 2016. Glacial onset predated Late Ordovician climate cooling. Paleoceanography 31, 800-821.
Porębska, E., Kozłowska-Dawidziuk, A., Masiak, M., 2004. The lundgreni event in the Silurian of the East European Platform, Poland. Palaeogeography, Palaeoclimatology, Palaeoecology 213, 271-294.
Rohling, E.J., 2013. Oxygen isotope composition of seawater. The Encyclopedia of Quaternary Science. Amsterdam: Elsevier 2, 915-922.
Royer, D.L., Donnadieu, Y., Park, J., Kowalczyk, J., Godderis, Y., 2014. Error analysis of CO2 and O2 estimates from the long-term geochemical model GEOCARBSULF. American Journal of Science 314, 1259-1283.
Slavík, L., Hladil, J., 2019. Early Devonian (Lochkovian – early Emsian) bioevents and conodont response in the Prague Synform (Czech Republic). Palaeogeography, Palaeoclimatology, Palaeoecology.

Trotter, J.A., Williams, I.S., Barnes, C.R., Lécuyer, C., Nicoll, R.S., 2008. Did Cooling Oceans Trigger Ordovician Biodiversification? Evidence from Conodont Thermometry. Science 321, 550-554.
Trotter, J.A., Williams, I.S., Barnes, C.R., Männik, P., Simpson, A., 2016. New conodont δ18O records of Silurian climate change: Implications for environmental and biological events. Palaeogeography, Palaeoclimatology, Palaeoecology 443, 34-48.